CHAPTER 4. RESULTS AND DISCUSSION

4.1. Preliminary results on the steels A and B currently in production in South Africa as well as two imported steels C and D.

4.1.1.Objective

Steel A and B armour plates are currently produced by Mittal Steel (South Africa) and were considered as the reference steels for the development of the advanced armour plate steels for two reasons:

- the materials are known, they meet the ballistic requirements and have already been tested both in ballistic tunnel tests and in combat; and
- Steels C and D are imported and are also used occasionally in South Africa for ballistic protection as substitutes for the Steels A and B.

These four armour steels, therefore, served as benchmark steels for the development of the new advanced performance armour steel RB600. A good understanding of the differences in ballistic performance of these four steels constitutes the basis for the desired improvement. Moreover, the industrial implementation of the metallurgical processes for the manufacture of the new RB600 armour steel, may be economically justified if the processing parameters remain close to those currently applied for the manufacture of steels A and B as armour plate.

4.1.2. Methodology

The specifications for armour steel plate in South Africa are actually formulated in terms of mechanical properties, i.e. hardness, yield strength, tensile strength, elongation of a 50 mm gauge length and assessed by ballistic tests. Amongst these specifications the hardness of the steel is considered to be the main indicator of ballistic performance. This design approach has been considered as an hypothesis in the first step for the characterisation of these steels. The attempt to maximise the hardness of these four armour steels has been established through water quenching of austenitised samples. More investigations based on the chemical compositions, dilatometric analyses, carbon extraction replicas and thin foil transmission electron microscopy have revealed some significant microstructural differences between steels A, B, C and D armour plates.

4.1.3. Results

4.1.3.1. Dilatometric analysis

a) Principle of the determination of the Ac_1 and Ac_3 temperatures

The 2 mm thick samples were slowly heated from room temperature to 900°C at a constant rate of 2°C per minute. The cooling down to room temperature was also done at the same rate. The useful part of the heating curve was then isolated for accurate reading of the A_c temperatures as schematically presented in the following figure:

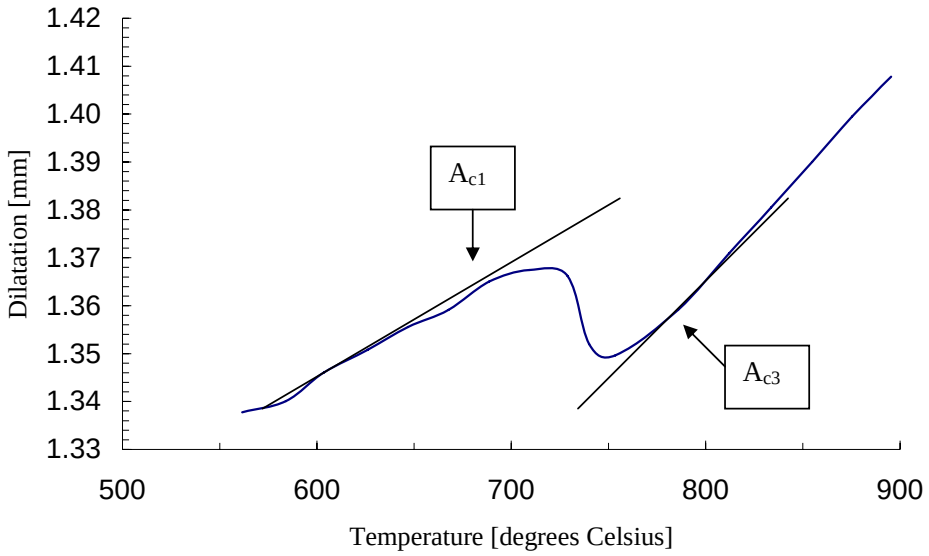

Figure 4.1.1. Illustration of reading off of the A_c temperatures on the heating curve of steel E

b) Principle of the determination of the M_s temperature

The M_s temperatures are read off from faster cooling rate curves. The 2 mm thick samples were heated up to 800°C, 850°C, 900°C or 950°C at a constant rate of 2°C per minute, soaked for 5 minutes and then quenched in a flow of Helium at a cooling rate higher than 200°C per second to form martensite. A typical dilatation curve is presented in figure 4.1.2. The determination of the martensite finish temperature by this technique is not accurate because it is difficult to determine the exact point of contact between the cooling curve and the straight-line tangent. Here the tangent is considered to be parallel to the first part of the heating curve. The measured transformation temperatures, for steel A to D are presented in table (4.1.1)

Table (4.1.1). Transformation temperatures measured by dilatometric analysis

	Ac_1 [°C]	Ac_3 [°C]	M_s [°C]
Steel A	698	758	285
Steel B	704	764	253
Steel C	702	742	241
Steel D	694	748	243

From these results the minimum austenitisation temperature was determined by adding 50°C (at least) to the Ac_3 temperatures, leading to about 800°C as a minimum.

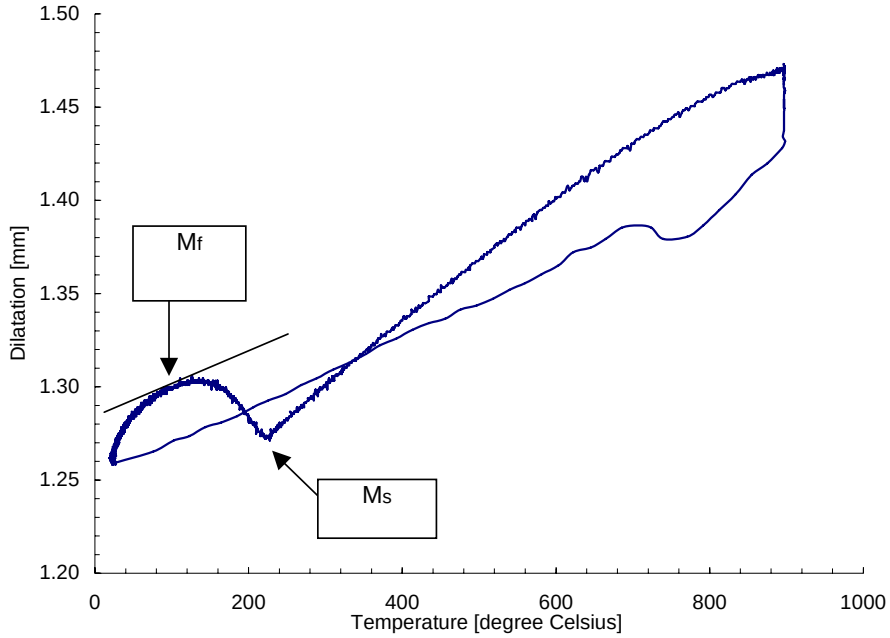

Figure 4.1.2. Determination of the M_s and M_f temperatures

4.1.3.2 . Quenching and tempering of Steel B

The average hardness of 8.5 mm thick steel A and that for 30 mm thick steel B armour plates after quenching and tempering, were found to be 520 VHN and 390 VHN respectively. The hardness profiles of both steels A and B produced lower hardnesses than the specified range of 640 VHN to 750 VHN, or a minimum of 600 BHN as specified for the RB600 armour steel to be developed.

Samples of Steel B were austenitised at 800°C, 850°C, 900°C and 950°C for 20 minutes, quenched into brine and then tempered at low temperatures varying between 170°C and 250°C. This ideal quench was used to determine the maximum hardness achievable for this steel. The initial material was received in 30 mm thick plates with a hardness of 378 VHN to 400 VHN. The highest hardness value obtained after the above ideal quench was 543 VHN, i.e. well below the specified minimum.

These results are plotted in Figure 4.1.3. At low tempering temperatures of between 170°C and 200°C**,** the effect of the tempering treatment on the hardness is more pronounced within the first hour. The hardness is very sensitive to the tempering temperature for a given tempering time.

Table (4.1.2). Hardness values of Steel B after austenitisation at 850°C, water-quenched and low-temperature tempering

	Vickers hardness after tempering at these temperatures		
Tempering time [hr]	170°C	200°C	250°C
0	543	543	543
0.5	540	500	481
1	520	502	481
4	502	508	473
11	511	484	436
24	499	481	449

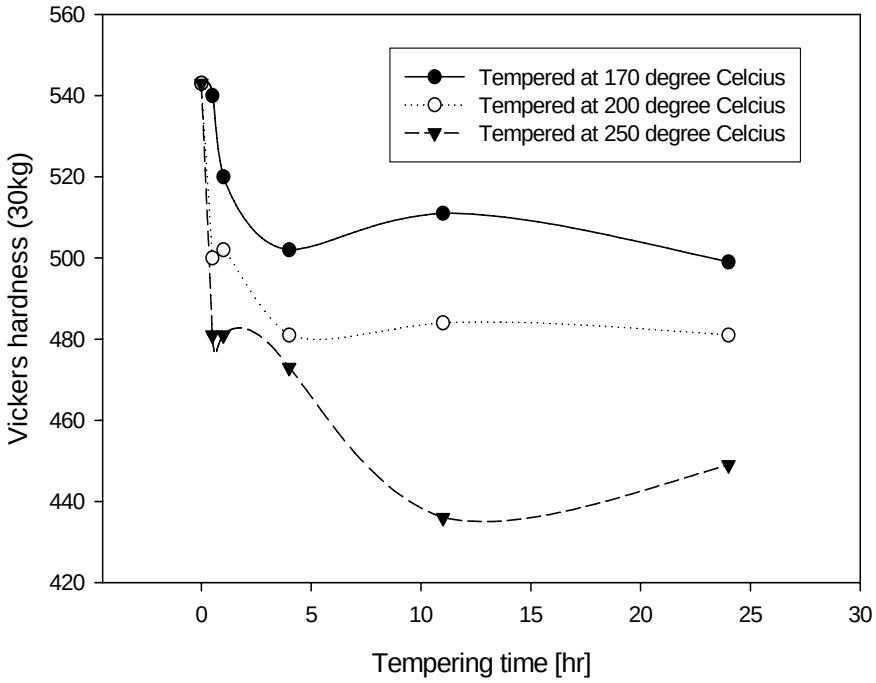

Figure 4.1.3. Vickers hardness of Steel B after austenitisation at 850°C for 20 minutes, water-quenching and tempering

An increase in the austenitisation temperature to 900°C or to 950°C does not alter this general behaviour, but rather determines the highest hardness achievable as shown in Figure 4.1.4. After austenitisation at 900°C and water-quenching, the Vickers hardness of steel B is slightly higher than the one obtained after austenitisation at 850°C**,** but the corresponding decrease in hardness during tempering is faster as shown in Table (4.1.3).

The austenitisation treatment at 950°C for 20 minutes produced a lower hardness in the as-quenched condition. The maximum Vickers hardness obtained for Steel B, was only 454 VHN in this case. That is almost equal to the hardness in the as-received condition.

Table (4.1.3). Vickers hardness of Steel B after austenitisation at 900°C, water-quenching and tempering

Time [hr]	VHN hardness after tempering at these temperatures		
	170°C	200°C	250°C
0	557	557	557
0.5	527	508	429
1	517	465	429
4	481	467	462
11	454	454	459
24	454	454	462

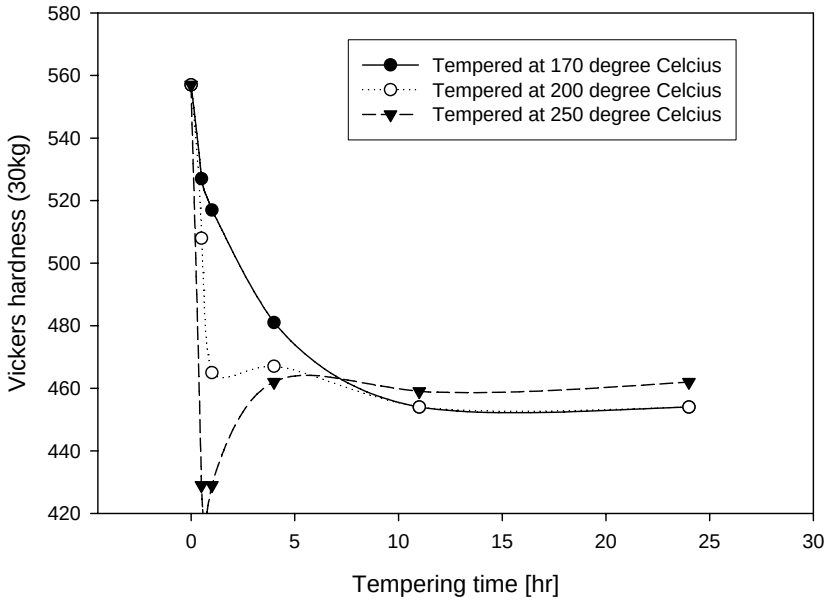

Figure 4.1.4. Vickers hardness number of steel B austenitised at 900°C for 20 minutes, water-quenched and tempered.

Carbon extraction replica transmission electron microscopy of the as-received steel B, revealed a significant volume fraction of coarse carbides formed on ferrite grain boundaries. The semi-quantitative analysis of the carbide particles by X-ray diffraction showed that these coarse particles contain Iron, Chromium, Manganese and Vanadium, whereas the finer particles contain mainly Titanium and Vanadium with less Chromium,

Manganese and Iron. The coarse carbide particles formed consistently during the tempering of the 30 mm thick plates of steel B at 590°C. The Titanium particles were inherited from the steel making process and would necessitate a very high solution temperature (and for a long time) to dissolve before quenching. This will cause grain growth with its detrimental effect on the subsequent toughness of the armour plate. Therefore, from a direct comparison of the locally produced steel B with the imported steel C, it appears that the Titanium and Vanadium should be reduced to the lowest level in these steels, and the tempering temperature should be low to prevent diffusion of the alloying elements and the subsequent formation of the corresponding carbide. To avoid excessive grain growth, however, in a Ti-free steel, the austenitisation times should be kept as short as possible.

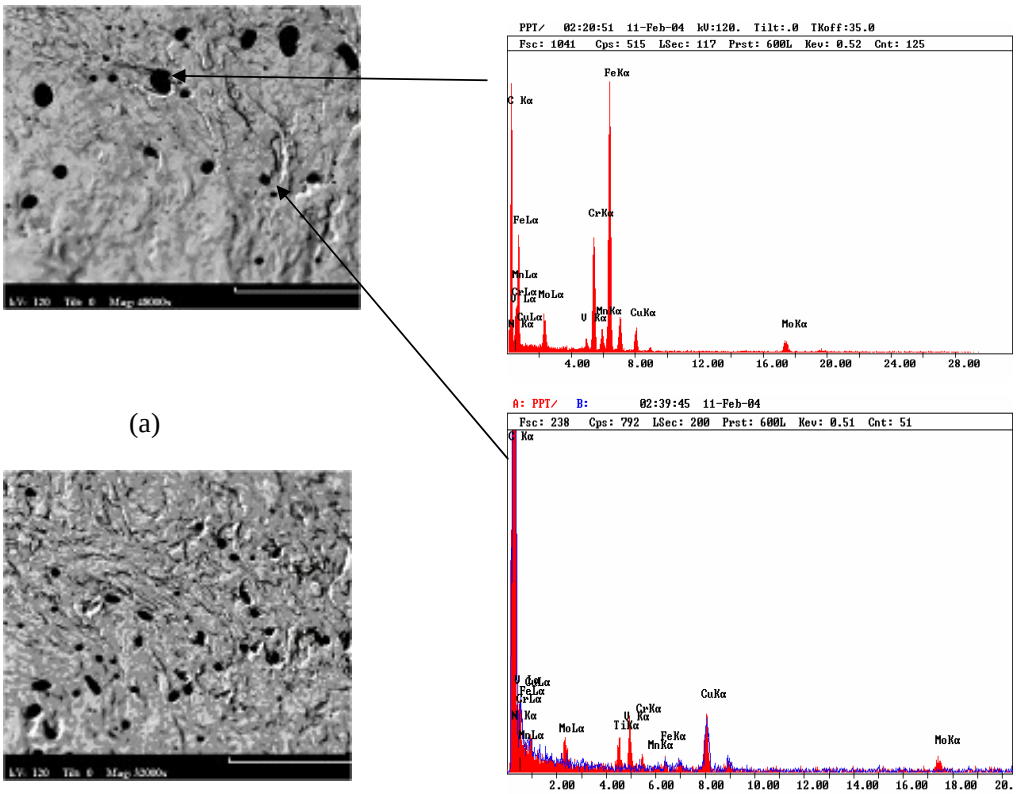

(a)

(b)

Figure 4.1.5. (a), (b) Carbon extraction replica transmission electron microscopy of a 30 mm steel B armour plate austenitised at 910°C , water quenched and tempered at 590°C for 38 minutes (label scale length = 10 microns)

4.1.3.3. Dilatometric analysis, quenching and tempering of steel C

From the experience at Mittal Steel (South Africa), the imported steel C has superior ballistic properties than the locally produced steel B. The hypothesis of the existence of a relationship between the microstructure and the ballistic performance of an armour steel, suggests that the difference in ballistic performance between these two steels may be established from their differences in microstructures.

The mechanical properties and microstructure of steel C have, therefore, been used as the minimum requirement for the new RB600 armour steel. The specifications for the steel C are given in Table (4.1.3).

Table (4.1.4). Specifications for steel C

	BHN	$YS_{0.2\%}$ [MPa]	UTS [MPa]	Charpy impact energy at-40^{0}C[Joule]	Minimum elongation [%] on a 50 mm gauge length
Steel C (specification)	570 – 640	1500	2000	12	5
Steel C (actual)	573 – 632	1400	2000	18	6

The transformation temperatures of steel C were determined by dilatometry and are reported in Table (4.1.1). A typical slow heating curve of steel C is shown in Figure 4.1.6(a), and the fast cooling curve for the determination of its M_S is shown in Figure 4.1.6(b).

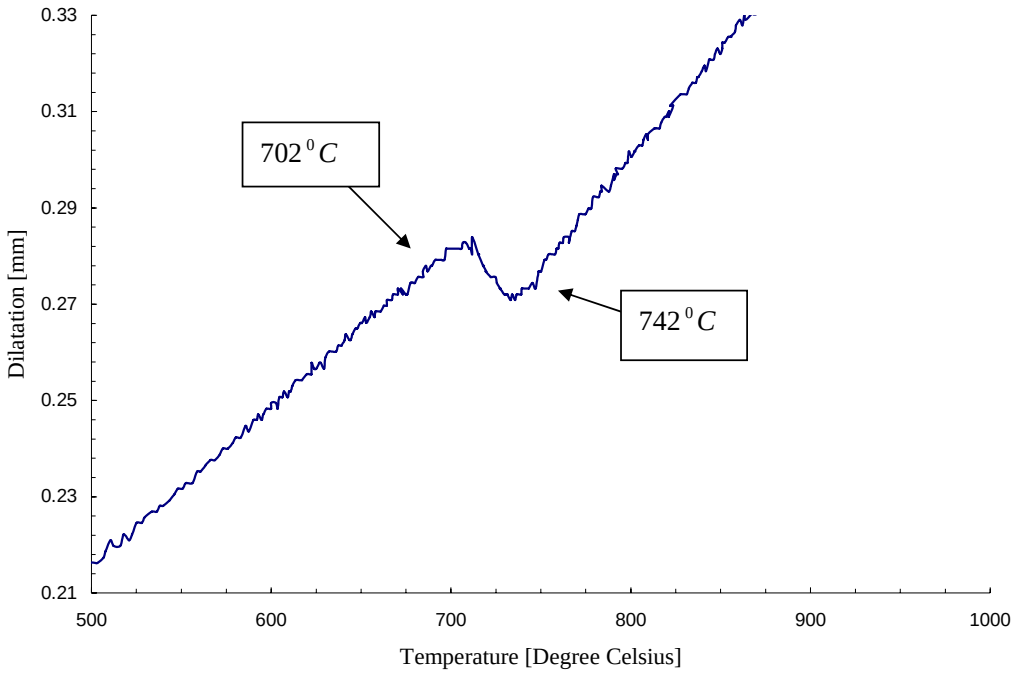

Figure 4.1.6(a): Slow heating curve of Steel C showing it's A_c transformation temperatures

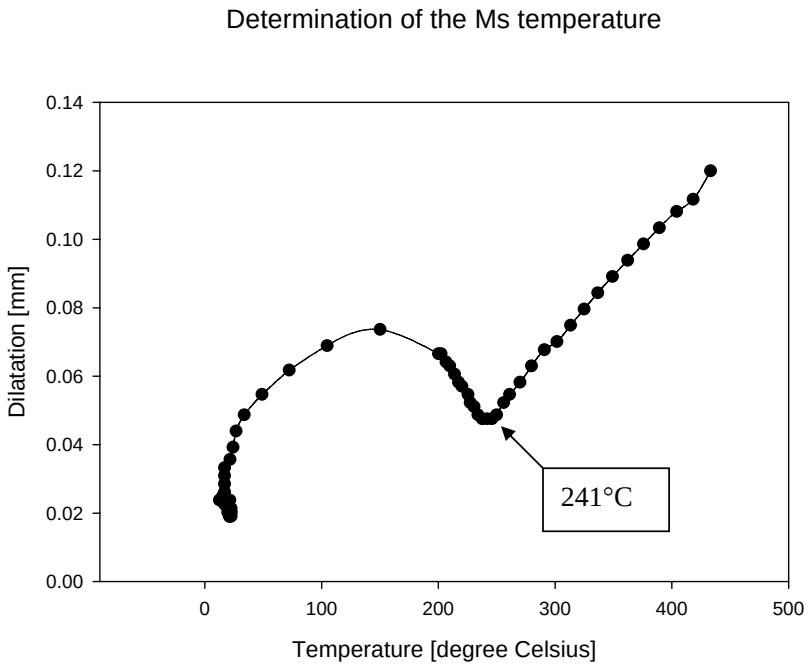

Figure 4.1.6(b) Fast cooling curve of steel C and reading off of the M_s temperature**.**

4.1.3.3.1. Hardness of steel C

The measurements of the Vickers hardness along four traverse lines crossing the 6.7 mm thick plate of steel C, are given in Table (4.1.5).

Table (4.1.5). Hardness profile of the 6.7 mm armour steel C plate

Depth from the surface [mm]	VHN 30[kg/mm^2]			
	Cross-line 1	Cross-line 2	Cross-line 3	Cross-line 4
0.5	652	648	618	639
1.5	680	661	657	666
2.5	631	635	644	637
3.5	614	622	644	627
4.5	635	626	652	638
5.5	648	626	622	632
Average	643	636	640	640
Std dev%	3	2	2	2

Steel C produced a Vickers hardness of 640 VHN with a standard deviation of 3%. Steel C is, therefore, harder than steel B. It also appears that steel C has a more consistent hardness through its cross section, which suggests the presence of a harder homogeneous microstructure. Nevertheless the hardness profile shows a relative maximum at about 1.5 mm below the outer surface and a relative minimum at a depth of about 3.5 mm on each of the four cross - lines.

This hardness profile indicates a relatively harder microstructure near the outer surface than near the inner surface, probably due to a difference in cooling rate on either side during the quench. The outer surface would, therefore, present a higher resistance to penetration in a ballistic test while the inner surface would be more resistant to spallation. Within the first 0.4mm depth from the outer surface, the Vickers micro hardness drops below 446 HV, probably due to some decarburisation during austenitisation. Near the other surface the micro hardness remains above 600 HV. This surface will, therefore, be better as the outer surface of the protective structure.

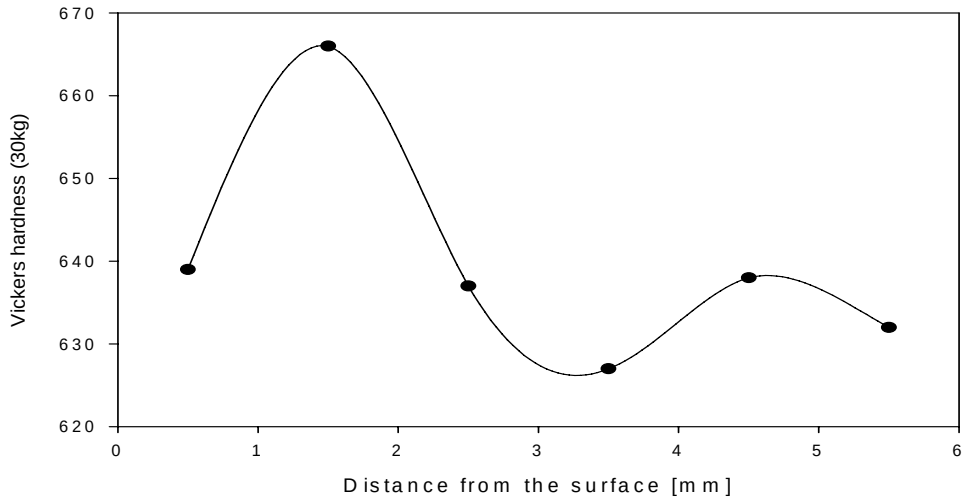

Figure 4.1.7. Transverse average hardness profile of Steel C

To explain the transverse hardness profile, two hypotheses were made. The first hypothesis is a possible segregation and a non-uniform distribution of alloying elements along the four hardness cross-lines. A cross-line semi-quantitative analysis with the scanning electron microscope did not reveal any major or measurable segregation of the main alloying elements, as may be seen in Figure 4.1.8, where the approximated weight percentages of the alloying elements determined by X-ray diffraction may be read off from the y-axis.

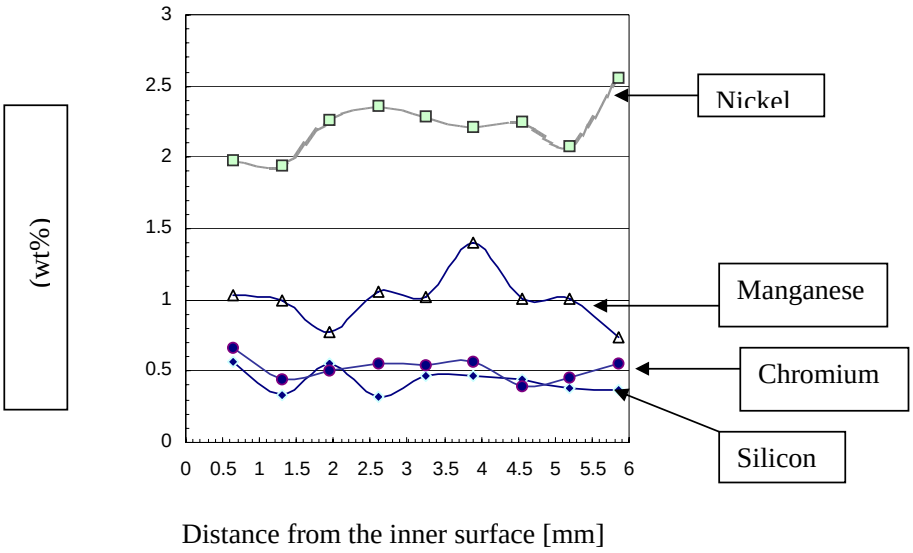

Figure.4.1.8. Alloying element distribution along a cross-line of Steel

The second hypothesis that was tested, is a possible fine precipitation of some carbides on grain boundaries during cooling after hot-rolling or during the tempering treatment. Such a precipitation can lead to some degree of depletion in Carbon within some areas. The assessment of this hypothesis is presented in the next section in Figure 4.1.10, by means of carbon extraction replica transmission electron microscopy.

.

4.1.3.3.2. Microstructure of steel C

The microstructure of steel C consists of a fine-grained martensite as shown Figure 4.1.9, by scanning electron microscopy. The resolution of optical microscopy was not enough to resolve this fine microstructure and, therefore, backscatter scanning electron microscopy was used for this purpose. Through the use of this SEM technique, it was not possible to confirm the presence of bainite in the martensitic microstructure. The grain size of steel C, as measured by SEM, varies between 8 and 10 micrometers. The grain boundaries and the precipitates were unresolvable because of their small sizes of less than 2 micrometers.

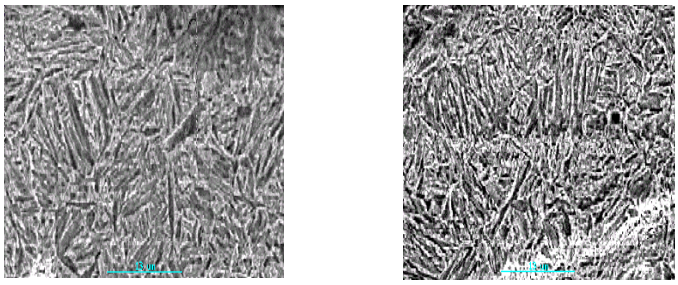

(a) (b)

Figure. 4.1.9. Microstructure of the 6.7 mm thick Steel C plate. Scanning electron micrographs at (a) 2.5 mm and (b) 3.5 mm depth into the plate.

The microstructure of this steel is a fine and homogeneous martensite throughout the cross section of the 6.7 mm plate. This fine microstructure may partially explain the higher hardness, combined with the higher toughness of steel C compared to steel B since it is well known that the microstructure predetermines the mechanical properties as assumed in the table below.

Table (4.1.6). Relationships in microstructure – mechanical properties

	Properties	**Controlling parameters**
Martensite	High hardness, high strength	Carbon and Manganese contents, austenitisation temperature and time, quench rate
Fine microstructure	highly defected substructure, retained austenite, fine precipitates	Nickel content, austenitisation temperature, cooling rate
Homogeneity	No stress raisers, high impact energy	Sulphur, Copper and Silicon contents, austenitisation temperature, cooling rate, tempering parameters

Figure 4.1.10 reveals no coarse carbide particles through carbon extraction replica transmission electron microscopy of sections taken at different depths below the outer surface. Contrary to steel B, the grain boundaries of steel C are without any carbides. Its matrix has finely dispersed particles of Titanium carbides and Titanium nitrides and these contain less Chromium and Manganese as in Steel B. There was also no measurable coarsening of the fine Titanium carbide and nitride particles during the tempering treatment, as was observed in steel B. A lower-temperature tempering for a shorter time of steel C may be the reason of the observed no coarsening of those particles.

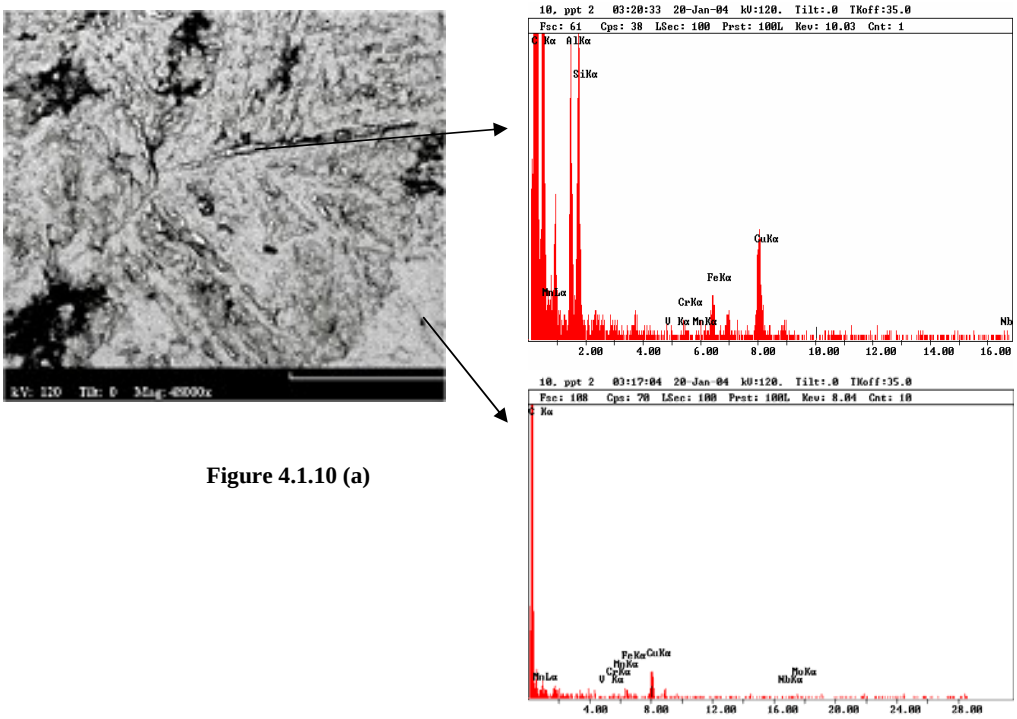

Figure 4.1.10 (a)

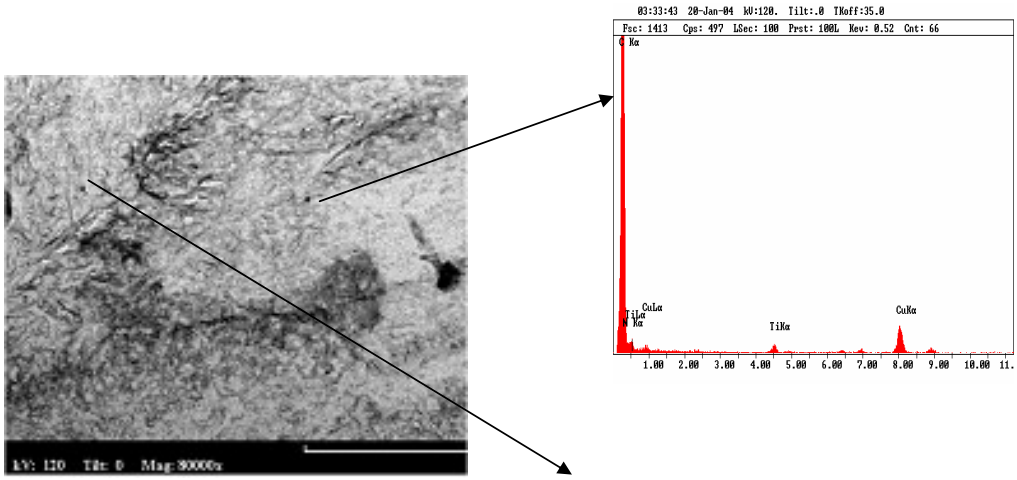

Figure 4.1.10 (b)

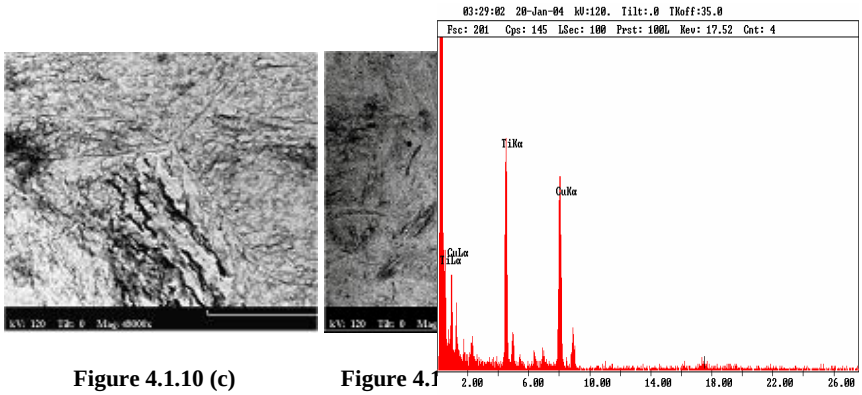

Figure 4.1.10 (c) **Figure 4.1**

Figure 4.1.10. Carbon extraction replica transmission electron micrographs and dark field images showing very fine carbides and nitrides within the matrix
(a): TEM carbon extraction replica at a depth of 0.5 to 1.5 mm from the surface;
(b) and (c): TEM extraction carbon replicas at a depth of 1.5 to 2.5 mm from the surface showing precipitate-free grain boundaries and small Titanium carbides and nitrides within the matrix.
(d): TEM extraction carbon replica at a depth of 3.5 to 4.5 mm from the surface revealing more fine particles than at depths of 1.5 mm and at 2.5 mm from the surface. (label scale length = 10 microns)

Thin foil transmission electron microscopy of Steel C in the as-received condition and an optical micrograph of a sample after a high-temperature tempering at 600°C for 30 seconds, are presented in figures 4.1.11 (a), 4.1.11 (b) and 4.1.12.

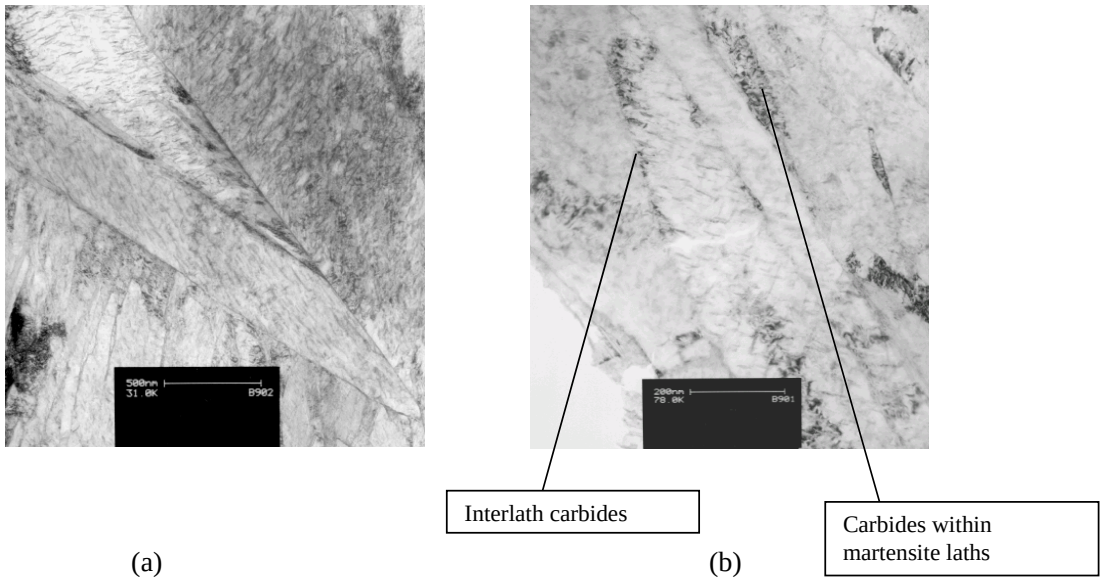

Figure 4.1.11. Thin foil transmission electron microscopy of Steel C in the as-received condition.

Figure 4.1.11 (a) and (b) show fine elongated carbides within the martensite laths of Steel C and slightly round carbide particles on and near the lath interfaces. The optical micrograph of the sample tempered at 600°C presents a microstructure composed of ferrite and coarse carbide particles, with a lower hardness.

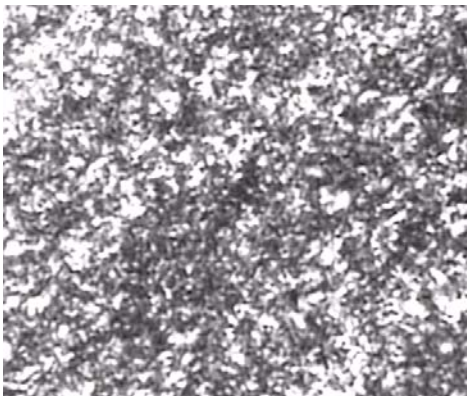

Figure 4.1.12. Optical micrograph of the Steel C after tempering 30 seconds at 600°C (magnification x1000).

Tempering of Steel C at 600°C for 30 seconds already softened the material to a hardness well below the specification. The hardness values of Steel C corresponding to the microstructures in figure 4.1.11 and figure 4.1.12 are compared in table 4.1.7.

Table (4.1.7). Vickers hardness of Steel C as-received and after tempering at 600°C.

	Figure No.	Vickers hardness
As-received	4.1.10 (a) and 4.1.10 (b)	640
850°C for 20 minutes		652
900°C for 20 minutes		661
Tempered at 600 ^{0}C for 30 seconds	4.1.11	446

The hardness values of Steel C after austenitisation at 850°C and 900°C followed by water-quenching to room temperature, are slightly higher than in the as-received condition, as shown in Table 4.1.7. The difference in Vickers hardness between the austenitised and then water quenched sample, and the as-received Steel C armour plate, is about 20 VHN units, confirming the presence of a low-temperature tempering applied to this steel, contrary to the high-temperature-tempering applied to Steel B. After tempering at 600°C for 30 seconds, the martensitic microstructure is completely transformed into a structure consisting of ferrite and carbides have also formed, as shown in figure 4.1.11. This structure had a hardness of only 446 VHN, far below the specified range for Steel C which is 660 to 720 VHN or 580 BHN to 640 BHN.

Simulation of water quenching of a 6 mm and a 8 mm plate of Steel C, was performed in the THETA dilatometer using a flow of Helium as coolant.
This was done to assess the efficiency of the industrial quenching process. After this simulation the Vickers hardness varied between 661 VHN and 671 VHN, which is in the same range of the Vickers hardness obtained after water quenching and higher by 30 units than the hardness of the as-received 6.7 mm Steel C armour plate. This again confirms the effectiveness of a low-temperature tempering treatment for a short time as was apparently applied in the case of Steel C armour plate. Figure 4.1.13 presents the three simulation curves superimposed on six experimental cooling curves of water quenching in the Mittal plant of steel bars and plates. The legend attached to the curves may be read as: 13B8P WQ designates the cooling curve for a 13 mm bar or a 8 mm plate, water-quenched to room temperature.

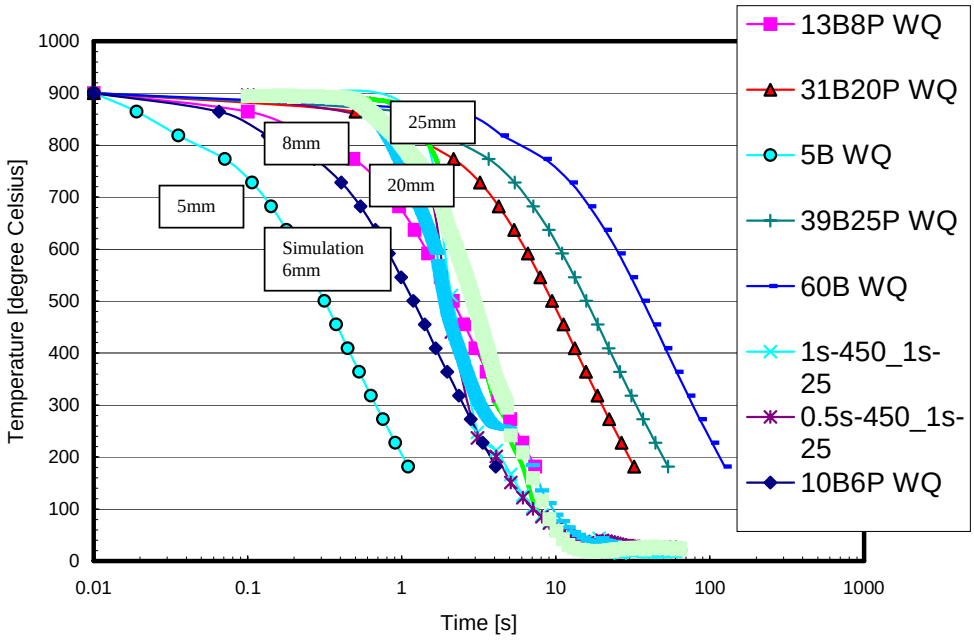

Figure 4.1.13. Three simulation curves of the water quenching of Steel C plates superimposed on 6 experimental cooling curves of industrial water quenching of plate steels in the Mittal plant.

The simulation samples were austenitised at 900°C for 10 minutes before being quenched in a flow of Helium according to the three simulation curves in °C versus time (in seconds) above.

4.2. Proposed design for an advanced RB600 armour plate

From these experiments it appears that the highest achievable hardness with steel B under the specified conditions, is 557 VHN. This hardness is reached through austenitisation at 900°C for 20 minutes and a water-quench to room temperature. The relatively low Carbon content of 0.3%C is the main barrier to the improvement in hardness of Steel B to values up to 640 VHN or 600 BHN after quenching, as required by the specification. Extraction carbon replica transmission electron microscopy has revealed that the high-temperature tempering at 590°C for more than 38 minutes (as was applied to Steel B armour plates) led to the precipitation of coarse carbides and to undesirable heterogeneities in the microstructure that alter the ballistic performance negatively. The coarse carbide particles are potential stress-raisers and reduce the nominal stress for effective resistance to impact loading. A low-temperature tempering should be considered to avoid this effect. Moreover, preliminary experiments have also shown that the hardness decreases by 10% to 25% of its initial value in the as-quenched condition when a low-temperature tempering between 170°C and 250°C is applied to both steel B and C armour plates.

A good armour martensitic steel should, therefore, have a fine and homogeneous microstructure consisting of a low temperature tempered martensite. Furthermore, such material must be clean with neither inclusions nor carbide precipitates on grain boundaries.

The following hypotheses have, therefore, been formulated for the development of an advanced armour plate steel with a superior ballistic performance:

1. to slightly increase the hardness and the strength of the martensitic steel through a moderate increase of the Carbon content to between 0.38%C and 0.43%C;
2. to prevent quench-cracking in the plates by adding Manganese in the range of 0.8 % to 2 %Mn;
3. to prevent or to delay the precipitation of cementite or any M_3C precipitates by adding Silicon and Chromium within the range of 0.4 % to 1.5 %;
4. to austenitise between 80°C 0 and 950°C for less than 60 minutes to prevent austenite grain growth;
5. to temper the armour plate below 250°C for less than 60 minutes for the necessary reduction of quench residual stresses for an increase of the toughness of the martensitic microstructure;
6. the Sulphur content should ideally be kept below 0.005%S to prevent the formation of Manganese sulphide particles that may act as stress raisers; and
7. the Titanium and Niobium contents should ideally be kept lower than 0.005%.

These seven hypotheses formed the basis for designing the first five high-performance armour steels. In practice, however, slight deviations from some of these “ideal” limits were found in some of the experimental alloys. These slight deviations appeared, however, not to be critical to the main hypotheses by which the alloy’s compositions were selected. The optimisation of their mechanical properties, microstructures and their ballistic performances are presented in the next paragraph.

4.3. Optimisation of the mechanical properties.

4.3.1. The optimisation problem

Until now, the hardness of armour plate was considered to be the decisive criterion in predicting the ballistic performance of the steel as it is supposed to indicate the ability of the target to withstand the impact of the projectile. Other design specifications for ballistic steels are based on the true strength to fracture and the resistance to spallation upon high velocity and hypervelocity impact that induces a high strain rate in the target. It appears that one possible approach in designing an advanced performance armour steel, defined here as RB600, would consist of a constrained optimisation problem of the hardness, the objective function, with two constraint functions, i.e. the tensile strength and the impact energy. Another design philosophy would specify an optimum constrained minimum of the objective function defined by the ratio YS/UTS of the candidate armour steel with two constraint functions, namely the Charpy impact energy at -40°C and the tensile strength at room temperature which is an indication of the true fracture strength of these steel.

It may be shown that the ratio YS/UTS is proportional to $(n)^n$, where n is the Hollomon work hardening exponent, by the relationship $\frac{YS_{(0.2)}}{UTS} = \left(\frac{e \times 0.2}{n}\right)^n$. The Hollomon work hardening exponent n, defines the ability of the material to resist instability in strain as found in the localisation of plastic deformation. The function $\frac{YS_{(0.2)}}{UTS}$, therefore, may define the objective function that must be minimised to meet the ballistic requirements, because this ratio decreases when n increases as $n < 1$.

It was noted in Chapter 2 that adiabatic conditions prevail in the impacted region during ballistic testing and the localised temperature may exceed 700°C, which is far above the testing temperature at which the mechanical properties are commonly measured for ballistic materials. At 700°C, phase transformations may occur that modify the microstructure and the mechanical properties of the armour steels. It is, therefore, necessary to finally assess the ballistic performance of the armour steels by ballistic testing to assure conformation with the requirement for military and security standards. The analysis of the localised microstructures of the armour steels before and after ballistic testing will, therefore, become a vital tool for understanding the relationship between the microstructures, the mechanical properties and the ballistic performance. The following methodology was, therefore, followed in the design of the advanced RB600 armour plate steel:

- design the first five alloys and their heat treatment based on the industrial and metallurgical understanding of the current armour steels B and C;
- solve the constrained optimisation problem of the mechanical properties in terms of four *independent variables*; viz. the austenitisation temperature, the tempering temperature, the tempering time and the chemical composition and one *dependent variable*, the martensite start temperature;
- predict the ballistic performance of the armour steels using three different criteria based on the hardness, the Ballistic Performance Index (BPI) [6], (quoted in paragraph 2.2.4), and the ratio YS/UTS;

- perform the ballistic testing according to the ARMSCOR specification for military applications and assess the validity of the specification;
- analyse the microstructures and other features of the martensitic steels;
- understand and explain the metallurgical reasons for the high as well as the low performances; and
- redesign a range of new alloys and their heat treatment parameters and repeat steps 3 to 6 of the above methodology scheme.

4.3.2 The chemical composition

Based on the hypothesis formulated in section 2.8 and the conclusion after the orientation tests in section 4.2, five steels, namely, steels E, F, G, H and I whose chemical compositions are given in Table (4.3.1), were vacuum melted in 5 kg casts each, hot rolled, heat treated and tested mechanically as well as ballistically. The tensile tests were performed at room temperature whereas the Charpy-V impact energy of the sub-sized specimens (due to limitations on the plate thicknesses) was measured at -40°C. The hot rolled plates were austenitised for 20 minutes at different temperatures and tempered for different times up to two hours, also at different temperatures, as described in section 4.3.3.

Table (4.3.1): Chemical compositions (wt%) of the first five high performance armour steels

	C	Mn	P	S	Si	Cu	Ni	Cr	Mo	V	Nb	Ti	N
Steel E	0.39	1.22	0.008	0.003	0.21	0.10	2.99	1.49	0.5	0.006	0.002	0.003	0.0049
Steel F	0.39	0.65	0.017	0.009	0.8	0.23	2.8	0.22	0.24	0.003	0.006	0.01	0.0051
Steel G	0.37	0.40	0.016	0.011	0.43	0.33	2.3	0.24	0.3	0.006	0.006	0.009	
Steel H	0.37	1.15	0.015	0.011	1.06	0.14	3.8	0.52	0.43	0.008	0.008	0.007	0.0036
Steel I	0.34	0.39	0.019	0.012	0.40	0.32	2.43	0.27	0.37	0.009	0.009	0.008	

The martensite start temperatures of these steels were measured by dilatometry as described previously and are given in Table (4.3.2). The volume fractions of retained austenite in the respective alloys were determined by quantitative X-ray diffraction.

Table (4.3.2): Measured M_S temperatures [°C] and volume fractions of retained austenite after quenching of steels E through to steel I

	Designation of the Steel				
	Steel E	**Steel F**	**Steel G**	**Steel H**	**Steel I**
Ms temperature [°C]	196	255	271	210	309
Volume fraction of the retained austenite [%]	5	0.6	0.5	4	0.5

4.3.3. The heat treatment cycle

Tensile specimens and sub-sized Charpy specimens, whose dimensions are presented in paragraphs 3.6.2 and 3.6.3 respectively, were austenitised at temperatures ranging between 800°C and 950°C for 20 minutes, before being water-quenched to room temperature and tempered at relatively low temperatures between 150°C and 400°C for various times between 0 and 120 minutes. The low-temperature tempering treatment was motivated by the constraint on the hardness requirement which, as specified by ARMSCOR and Mittal Steel South Africa for the high performance armour steels, should be as high as 600 HBN or 640 VHN, and also by the abrupt drop of hardness to values lower than 450 VHN

observed on steels B and C when tempered above 200°C. However, to capture the effects of this softening behaviour, the effect of the tempering temperature on the mechanical properties was, therefore, studied over quite a large range, i.e. from room temperature to 400°C. Moreover, the effect of the heat treatment parameters on the ratio YS/UTS was analysed.

4.3.4. Variation of the mechanical properties

The variation of the yield strength to ultimate tensile strength ratio YS/UTS, the ultimate tensile strength and the Charpy impact energy of steels E through to I as a function of the austenitisation temperature and the tempering temperature, are first presented. This will be followed by a comparative analysis taking into account the differences in the martensite start temperatures of the candidate advanced performance armour steels. The optimisation problem is stated for each steel in terms of the objective function that needs to be minimised and two constraints. The three equations were determined for each of the five steels E through to I by surface fitting using EXCEL 2000 software. The three-dimensional plots of the surfaces and the projections of the isolines for the two-dimensional mapping of the optimum regions were performed using MATLAB 7.0.

From the experimental data it was observed that third degree polynomials could fit the results within the experimental ranges of the austenitisation temperature and the tempering temperature, with good accuracy. This led to the general mathematical expression of the surfaces representing the properties as follows:

- The austenitisation and tempering temperatures require normalisation to allow the computation and to provide the minimum rounding errors. It was found to be better to work with values within the same numerical range, i.e. –1 to +2 rather than using two different ranges for the austenitisation temperatures and the tempering temperatures. The normalised tempering temperature T_{tn} is defined, here, as follows:

$$T_{tn} = \frac{(T_t - T_{tm})}{(T_{tm} - 25)} \qquad (4.1)$$

where T_t is the actual tempering temperature in degrees Celsius, T_{tm} is a mean tempering temperature from $T_{tm} = \frac{25 + 300}{2}$ =162.5°C. Exactly how this normalised temperature is defined is not too important for the purposes of this study as the same trends will be found using a different normalisation definition.

- The normalised austenitisation temperature T_{an} is defined, here, as follows:

$$T_{an} = \frac{T_a - T_{am}}{T_{am} - 850} \qquad (4.2)$$

where T_a is the actual austenitisation temperature in degrees Celsius and T_{am} is the mean austenitisation temperature from $T_{am} = \frac{800 + 950}{2}$ =875°C.

➢ The particular mechanical property (MP) is then fitted by the surface fitting equation:

$$MP(T_{an}, T_{tn}) = a(T_{an}) \times T_{tn}^{\ 3} + b(T_{an}) \times T_{tn}^{\ 2} + c(T_{an}) \times T_{tn} + d \qquad (4.3)$$

where the fitting parameters a, b, c and d are polynomials in T_{an} and are of the general form:

$$p = A \times T_{an}^{\ 3} + B \times T_{an}^{\ 2} + C \times T_{an} + D \qquad (4.4)$$

where A, B, C and D are constant real parameters.

➢ Combining equations (4.3) and (4.4) gives a sixth order non-linear equation in the normalised temperatures T_{an} and T_{tn}:

$$MP(T_{an}, T_{tn}) = \left(A_1 \times T_{an}^{\ 3} + B_1 \times T_{an}^{\ 2} + C_1 \times T_{an} + D\right) \times t_{tn}^{\ 3} + \left(A_2 \times T_{an}^{\ 3} + B_2 \times T_{an}^{\ 2} + C_2 \times T_{an} + D_2\right) \times t_{tn}^{\ 2} + \left(A_3 \times T_{an}^{\ 3} + B_3 \times T_{an}^{\ 2} + C_3 \times T_{an} + D\right) \times t_{tn} + \left(A_4 \times T_{an}^{\ 3} + B_4 \times T_{an}^{\ 2} + C_4 \times T_{an} + D_4\right) \qquad (4.5)$$

Equation 4.5 is the mathematical presentation of the particular mechanical property to be considered in the optimisation problem. The optimisation techniques currently used apply to the optimisation of quadratic non-linear problems. It then becomes necessary in the present case to graphically solve the problem using two-dimensional projections of contours of equal height (i.e. iso-lines) to visualise the optimum regions in the normalised (T_{an}, T_{tn}) planes.

4.3.4.1 Mechanical properties of Steel E

a) Fitting function for the UTS

The results from the measurements of the ultimate tensile strength of steel E are presented in Table (4.3.3).

Table (4.3.3). Ultimate tensile strength of steel E (MPa)

		Ultimate tensile strength in MPa as a function of the austenitisation temperature [°C]			
Tempering temperature[°C]	**Normalised tempering temperature T_{tn}**	**800°C**	**850°C**	**900°C**	**950°C**
25°C	-1	1202	1456	1400	1436
150°C	-0.09091	1956	1767	1580	1524
200°C	0.272727	1935	1846	1472	1535
250°C	0.636364	1874	1609	1326	1484
300°C	1	1800	1320	1308	1317
350°C	1.363636	1553	1265	1173	1115
400°C	1.727273	1532	1202	1076	995

The surface fitting is done in two steps and the first one gives the estimate of the parameters required in Equation (4.3) at different austenitisation temperatures. The results of these calculations and the correlation coefficient R^2 for steel E are tabled below:

Table (4.3.4): The fitting parameters and the correlation coefficients in equation (4.3) for the ultimate tensile strength of steel E

Austenitisation temperature	Normalised austenitisation temperature	Fitting parameters in equation (4.3)				Correlation coefficient
		a	b	c	d	
800°C	-1	158.3	-488.26	112.67	1961.2	0.984
850°C	-0.33333	184.05	-410.62	-209.35	1832.6	0.939
900°C	0.333333	79.271	-201.67	-148.29	1537.3	0.965
950°C	1	12.683	-177.44	-67.755	1553	0.978

It appears that the parameters a, b, c and d are some function of the austenitisation temperature. The second step of the surface fitting process consists of determining the variation of each of these parameters in Table (4.3.4) with the normalised austenitisation temperature. The results of the calculations are tabled as follows:

Table (4.3.5): The fitting parameters and the correlation factors in equation (4.4) for the ultimate tensile strength of steel E.

	Parameters in equation (4.4)				Correlation coefficients
	A	B	C	D	
a	94.905	-51.94	-167.71	137.43	1
b	-177.77	-30.043	333.18	-302.81	1
c	-204.53	226.44	114.32	-203.98	1
d	268.71	81.169	-472.81	1675.9	1

The variation of the ultimate tensile strength of steel E with the normalised austenitisation and tempering temperatures may then be represented mathematically by the function:

$$UTS = \left(94.905T_{sn}^{\ 3} - 51.94T_{an}^{\ 2} - 167.71T_{an} + 137.43\right) \times T_{tn}^{\ 3} + \left(-177.77T_{an}^{\ 3} - 30.043T_{an}^{\ 2} + 333.18T_{an} - 302.81\right) \times T_{tn}^{\ 2}$$
$$+ \left(-204.53T_{an}^{\ 3} + 226.44T_{an}^{\ 2} + 114.32T_{an} - 203.98\right) \times T_{tn} + \left(268.71T_{an}^{\ 3} + 81.169T_{an}^{\ 2} - 472.81T_{an} + 1875.9\right) \quad (4.6)$$

b) Fitting function for the ratio YS/UTS

The determination of the function expressing the variable YS/UTS for steel E, also as a function of the austenitisation and tempering temperatures, is done by the same two-step process above that was used for the surface fitting of the ultimate tensile strength.

The results on the YS/UTS ratios from the tensile tests at room temperature on steel E are given in the Table (4.3.6). The calculated surface fitting parameters to be considered in Equations (4.3) and (4.4) for the YS/UTS ratio are shown in Tables (4.3.7) and (4.3.8).

Table (4.3.6): The YS/UTS ratio of steel E at room temperature, as a function of the austenitisation and tempering temperatures

		YS/UTS ratio as a function of the austenitisation temperature			
Tempering temperature	**Normalised tempering temperature**	**800°C**	**850°C**	**900°C**	**950°C**
25°C	-1	0.47	0.46	0.44	0.42
150°C	-0.09091	0.50	0.47	0.44	0.43
200°C	0.272727	0.53	0.49	0.45	0.46
250°C	0.636364	0.57	0.51	0.49	0.51
300°C	1	0.61	0.53	0.53	0.55
350°C	1.363636	0.64	0.55	0.57	0.59
400°C	1.727273	0.66	0.57	0.61	0.64

Table (4.3.7) The fitting parameters and the correlation coefficients in equation (4.3) for the ratio YS/UTS of steel E

		Parameters in equation (4.3)			
Austenitisation temperature	**Normalised austenitisation temperature**	**a**	**b**	**c**	**Correlation coefficient**
800°C	-1	0.0159	0.0632	0.5167	0.98
850°C	-0.33333	0.0098	0.0336	0.4816	0.997
900°C	0.333333	0.033	0.043	0.4444	0.993
950°C	1	0.0291	0.0635	0.4464	0.991

Table (4.3.8) : The fitting parameters and the correlation factors in equation (4.4) for the ratio YS/UTS of the steel E.

	Parameters in equation (4.4)				**Correlation coefficients**
	A	B	C	D	
a	-0.0317	0.0012	0.0383	0.0213	1
b	-0.0157	0.0282	0.0158	0.0352	1
c	0.0232	0.0209	-0.0584	0.4607	1

The variation of the YS/UTS ratio with the austenitisation and the tempering temperatures is then described by the function introducing the normalised temperatures T_{an} and T_{tn} expressed in Equation (4.7):

$$\frac{YS}{TS} = \left(-0.0317T_{an}^{\ 3} + 0.0012T_{an}^{\ 2} + 0.0383T_{an} + 0.0213\right) \times T_{tn}^{\ 2} + \left(-0.0157T_{an}^{\ 3} + 0.0282T_{an}^{\ 2} + 0.0158T_{an} + 0.0352\right) \times T_{tn} + \left(0.0232T_{an}^{\ 3} + 0.0209T_{an}^{\ 2} - 0.0584T_{an} + 0.4607\right) \quad (4.7)$$

c) Fitting function for the Charpy impact energy

Equation (4.7) is the objective function that needs to be minimised for steel E. Equation (4.6) is the first constraint on the system while the second constraint is taken from the Charpy impact energy of the sub-sized specimens tested at -40°C.

The fitting surface is obtained from the experimental values of the Charpy impact energy presented in Table (4.3.9). The fitting parameters for Equations (4.3) and (4.4) obtained by regression analysis, are given in Tables (4.3.10) and (4.3.11) respectively.

Table (4.3.9): Charpy impact energy (in Joules) of steel E (of the sub-sized specimens) tested at -40°C, as a function of both the austenitisation and the tempering temperatures

		Charpy impact energy (J) as a function of the austenitisation temperature			
Tempering temperature	**Normalised tempering temperature**	**800°C**	**850°C**	**900°C**	**950°C**
25°C	-1	6.9	5.9	4.9	4.9
150°C	-0.09091	7.9	6.9	5.9	4.9
200°C	0.272727	8.9	7.9	7.9	6.9
250°C	0.636364	10.8	8.9	7.9	6.9
300°C	1	12.8	9.8	8.9	7.9
350°C	1.363636	13.8	11.8	9.8	7.888
400°C	1.727273	13.8	12.8	11.8	10.8

Table (4.3.10: Fitting parameters of the Charpy impact energy of steel E, in Equation (4.3)

		Fitting parameters in (4.3)				Correlation coefficients
Austenitisation temperature	**Normalised austenitisation temperature**	**a**	**b**	**c**	**d**	
800°C	-1	-1.3036	1.8385	4.1496	7.946	0.995
850°C	-0.33333	-0.1717	0.925	2.2822	7.1079	0.995
900°C	0.333333	0.2342	0.2435	1.7912	6.648	0.97
950°C	1	0.293	0.4097	1.0982	5.808	0.906

Table (4.3.11): Fitting parameters of the Charpy impact energy of steel E, in Equation (4.4)

	Fitting parameters in (4.4)				Correlation coefficients
	A	**B**	**C**	**D**	
a	0.2131	-0.6036	0.5825	0.0983	1
b	0.3463	0.6073	-1.0607	0.5168	1
c	-0.8878	0.6606	-0.6379	1.9633	1
d	-0.4265	-0.0011	-0.6425	6.8781	1

The mathematical expression that fits the experimental Charpy impact energy may be written as:

$$CIE(-40^0C) = (0.2131T_{an}^{\ 3} - 0.6036T_{an}^{\ 2} + 0.5825T_{an} + 0.0983) \times T_{tn}^{\ 3} + (0.3463T_{an}^{\ 3} + 0.6073T_{an}^{\ 2} - 1.0607T_{an} + 0.5168) \times T_{tn}^{\ 2}$$
$$+ (-0.8878T_{an}^{\ 3} + 0.6606T_{an}^{\ 2} - 0.6379T_{an} + 1.9633) \times T_{an} + (-0.4262T_{an}^{\ 3} - 0.0011T_{an}^{\ 2} - 0.6425T_{an} + 6.8781) \quad (4.8)$$

Equation (4.8) is the second constraint of the system to be optimised.

Overall fitting

The optimisation problem may be written in classical form as follows:

$$\begin{aligned} YS/UTS &\le r_0 \\ UTS &\ge \Sigma_0 \\ CIE\,(\text{-}40°\text{C}) &\ge IE_0 \end{aligned} \qquad (4.9)$$

where r_0 is the boundary in the YS/UTS ratio yet to be determined after ballistic testing, Σ_0 is the current limit in UTS specified by ARMSCOR and is equal to 1700 MPa. The validity of this limit will be re-assessed later after the ballistic testing. CIE_0 is the minimum Charpy impact energy that indicates the resistance against spallation when the armour steel is impacted by a high velocity projectile at sub-zero temperatures. The ARMSCOR specification fixes this minimum at 13 Joules for full size Charpy specimen tested at -40°C. The optimisation problem represented in Equation (4.9) is shown graphically in Figure (4.3.1). From Tables (4.3.3), (4.3.6) and (4.3.9), it appears that a three-dimensional plot of the three functions that compose the system within the same axes, will require a scaling factor for visualisation of the problem. This is due to the fact that the absolute values of the YS/UTS ratio are very small compared to the ultimate tensile strength. A scaling factor of 2000 is, therefore, applied to the YS/UTS ratio and one of 100 to the Charpy impact energy function CIE (-40°C) before plotting. The effect of the scaling factors is only a translation of the fitting surfaces from lower to high values, but will still display the trends as before**.** The objective function YS/UTS is represented by the surface in between the ultimate tensile strength surface on top and the Charpy impact energy surface on the bottom. The feasible region as well as the optimum region are visualised by the use of the contours of equal values of the properties.

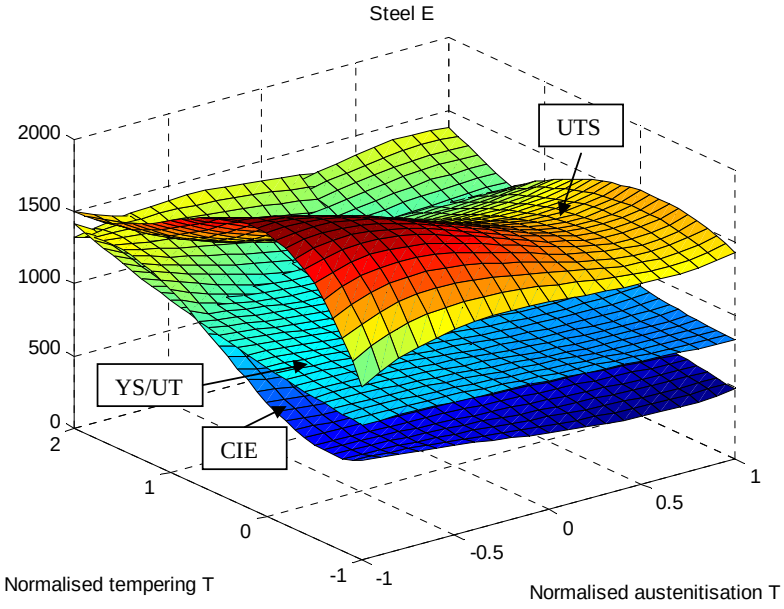

Figure 4.3.1(a): Three-dimensional representation of the YS/UTS objective function (surface in the middle), the UTS (upper surface) and the Charpy impact energy (lower surface)

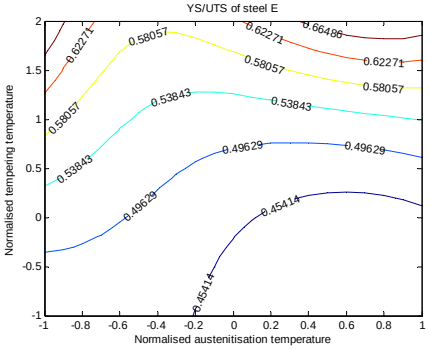

Figure 4.3.1(b): Contours of constant YS/UTS ratio for steel E

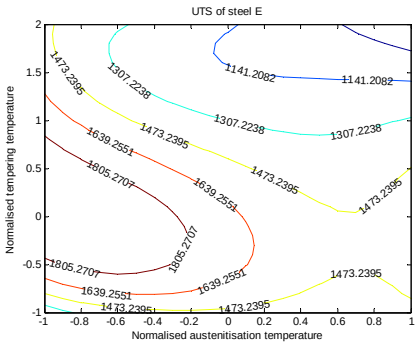

Figure 4.3.1(c): Contours of constant tensile strength (in MPa) of steel E

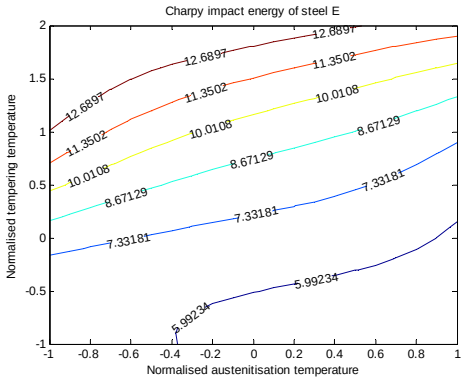

Figure 4.3.1(d): Contours of constant Charpy impact energy (in Joules) at -40°C for Steel E

From Figure 4.3.1(b), it appears that the optimum region for the YS/UTS ratio corresponds to the region of medium to high normalised austenitisation temperatures which lie between the normalised values of –0.6 to 1, or actually between 830°C and 950°C; together with low values of the normalised tempering temperatures, lying between the normalised values of –1 and 0.4, or actually lower than 217°C.

From Figure 4.3.1(c), it appears that a tensile strength larger than 1700 MPa is obtained for steel E when the normalised austenitisation temperature is lower than –0.1 or lower than actually 867°C and the normalised tempering temperature lies between the normalised values of –0.5 and 1, or actually between 95°C and 300°C. If the tempering temperature is lower than 95°C, the tensile strength would become difficult to determine because of the brittle behaviour of steel E in this condition. From Figure 4.3.1(d) a Charpy impact energy at -40°C that is higher than the specified 13 Joules, is obtained for the normalised temperatures between –1 and 0.2 or lower than the actual 890°C and the normalised tempering temperature is above 0.9 or actually 286°C. The summary of this discussion is presented in Table (4.3.12).

Table (4.3.12). Heat treatment conditions predicted to be favourable to the ballistic properties for steel E.

	Favourable conditions	
Property	**Austenitisation temperature**	**Tempering temperature**
Low YS/TS	830°C to 950°C	< 217°C
High UTS	< 867°C	95°C to 300°C
CIE(-40°C)	< 890°C	> 286°C

The optimum heat treatment region for steel E may be fixed in a first approach, at an austenitisation temperature between 830ºC and 900ºC. It is more difficult to find a compromise concerning the tempering temperature between the YS/UTS ratio and the Charpy impact energy at -40°C, as can be seen from the third column in Table (4.3.12). Predominance has been given to the ratio YS/UTS according to the design methodology chosen in Section 4.3.1; and the optimum tempering temperature is, therefore, fixed at below 200°C for steel E.

The hardness of steel E varies with both the austenitisation temperature and the tempering temperature. The results on the Vickers hardness of this steel are given in Table (4.3.13). The regression analysis and the surface fitting were developed following the same scheme as proposed earlier in this Chapter. It is to be noted that the hardness of steel E decreases very fast to values as low as 450 VHN when the tempering temperature is above 200°C. That would be very low compared to the value of 650VHN specified by ARMSCOR and Mittal Steel South Africa for their advanced performance armour steels.

Table (4.3.13): Variation of the Vickers hardness of Steel E with the austenitisation temperature and the tempering temperature.

	Vickers hardness as a function of the austenitisation temperature [^{0}C]			
Tempering temperature °C	**800°C**	**850°C**	**900°C**	**950°C**
25°C	560	590	630	620
150°C	550	545	550	610
200°C	490	450	450	545
250°C	460	422	430	520
300°C	440	415	420	500

The fitting parameters for the corresponding Equations (4.3) and (4.4) are contained in Tables (4.3.14) and (4.3.15) respectively.

Table (4.3.14): Fitting parameters for the Vickers hardness of Steel E, in Equation (4.3)

		Fitting parameters for (4.3)				
Austenitisation temperature	**Normalised austenitisation temperature**	**a**	**b**	**c**	**d**	**Correlation coefficients**
800°C	-1	75.755	-33.953	-135.13	534.8	0.992
850°C	-0.33333	44.411	-14.824	-116.57	532.79	0.998
900°C	0.333333	29	8.5389	-113.52	537.12	0.997
950°C	1	79.519	-32.044	-138.65	593.22	0.985

Table (4.3.15): Fitting parameters for the Vickers hardness of steel E, in Equation (4.4)

	Fitting parameters for (4.4)				**Correlation coefficients**
	A	**B**	**C**	**D**	
a	28.123	46.048	-26.241	31.589	1
b	-38.351	-33.588	39.306	0.5894	1
c	0	-24.576	-1.1265	-112.31	0.983
d	0	32.687	26.939	531.32	0.96

The variation of the Vickers hardness with the austenitisation temperature and with the tempering temperature is then written in terms of the normalised temperatures as follows:

$$HV = \left(28.123T_{an}^{\ 3} + 46.048T_{an} - 26.241T_{an} + 31.589\right) \times T_{tn}^{\ 3} + \left(-38.351T_{an}^{\ 3} - 33.588T_{an}^{\ 2} + 39.306T_{an} + 0.5894\right) \times T_{tn}^{\ 2} + \left(-24.576T_{an}^{\ 2} - 1.1265T_{an} - 112.31\right) \times T_{tn} + \left(32.687T_{an}^{\ 2} + 26.939T_{an} + 531.32\right) \quad (4.10)$$

The surface representing the Vickers hardness is presented in Figure 4.3.2(a), together with the plane for a hardness of 650VHN as specified by ARMSCOR and Mittal Steel South Africa. The plane for 550VHN is also shown in the same figure.

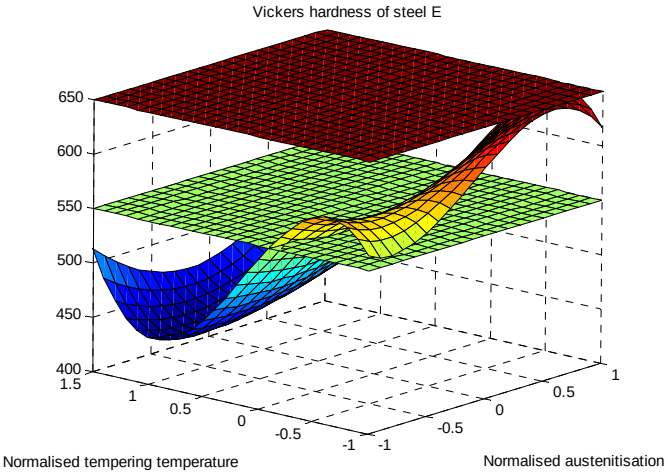

Figure 4.3.2(a): Variation of the Vickers hardness of steel E with the normalised austenitisation and tempering temperatures. The surface corresponding to the specified 650 VHN is shown together with one for 550 VHN.

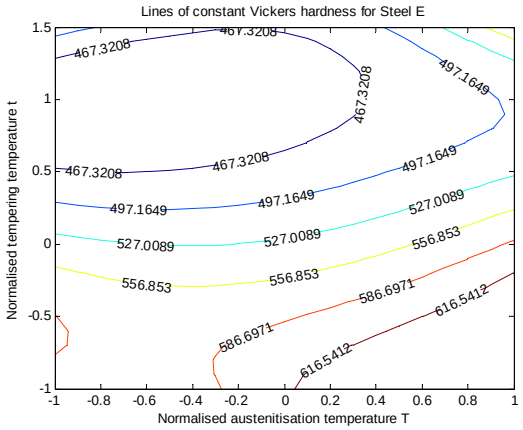

Figure 4.3.2(b): Lines of constant hardness corresponding to Figure 4.3.2.a.

The hardness of steel E in the quenched condition, is relatively constant when the austenitisation temperature is increased between 800°C and 900°C. Above this austenitisation temperature range, for instance at 950°C, however, the maximum hardness that was attained increased. This increase in hardness is mainly due to two factors; firstly the solid solution hardening of the parent austenite due to the increased dissolution of some carbides when the austenitisation temperature was increased and secondly, to a subsequent decrease in the M_S temperature leading to a harder untempered martensite with a greater amount of Carbon in solution.

At 950°C grain growth of the austenite may also become significant. The decrease in the martensite start temperature may, however, lead to an increase in the volume fraction of retained austenite and impose a limit on the increase in the average hardness of the steel. The grain size of steel E after austenitisation for 20 minutes, as determined by the line intercept method using the line scanning function of the scanning electron microscope, increased from $7.0 \pm 0.8\,\mu m$ when the austenitisation temperature was 850°C, to $10 \pm 0.8\,\mu m$ when the austenitisation temperature was 950°C.

It is to be noted in Table (4.3.12) that the higher tensile strength was achieved when the austenitisation temperature was below 867°C and it dropped again above this austenitisation temperature. This effect may also be related to grain growth and the increase in the volume fraction of the retained austenite. Therefore, it appears that both the tensile strength and the hardness increase with an increase in the austenitisation temperature, but the upper limit in the tensile strength occurs earlier than for the hardness. This apparent "disjunction" between the maximum hardness and UTS at a low austenitisation temperature for the former and at a high austenitisation temperature for the latter, may be related to the presence of retained austenite after a high austenitisation temperature which affects the different mechanical processes of hardness and tensile testing differently (due to different strain rates). A secondary effect may also arise from an increase in grain size at high austenitisation temperatures although this effect is probably relatively small due to a small increase in grain size from 7 to 10 μm.

The rate of decrease in hardness of steel E upon low-temperature tempering, appears to be slower when the austenitisation temperature is lower within the range from 800°C to 900°C**.** This trend indicates that at higher austenitisation temperatures the amount of Carbon dissolved into the parent austenite is high, which leads to a higher activity of Carbon in the martensite upon tempering. The sudden change of slope of the hardness curves in Figure 4.3.2(a) suggests the existence of two different mechanisms by which the martensite is softened within the considered tempering temperature range. The first softening mechanism is active below 150°C and the second mechanism, leading to a sharp drop in hardness, becomes active upon tempering between 200°C and 250°C. Tempering this armour steel between 200°C and 250°C leads to the coarsening of the metastable transition ε-carbides or η-carbides previously formed below 150°C and to their transformation into cementite.

The elongation upon tensile testing at room temperature increases when the tempering temperature is increased and it decreases when the austenitisation temperature is increased.

Table (4.3.16): Elongation of the 33 mm gauge length of steel E that was austenitised at 850°C and at 900°C respectively, water-quenched and tempered for 60 minutes.

	Tensile elongation (%) after austenitisation at these temperatures	
Tempering temperature	**850°C**	**900°C**
Water quenched	0.3	0.3
150°C	4.5	3.5
200°C	7	4.5
250°C	8.5	5.8
300°C	8.5	6.5

4.3.4.2. Mechanical properties of steel F

The optimisation problem for the candidate armour Steel F was established in the same manner than was done for steel E. The fitting parameters and final equations are given in Appendix A2 and only the graphical presentation is given here.

The optimum region for the predicted ballistic performance of this steel is discussed later in comparison with the optimum region for its mechanical properties.

Table (4.3.17): The yield strength to the tensile strength ratio of steel F.

		YS/UTS ratios as a function of the austenitisation temperature			
Tempering temperature	**Normalised tempering temperature**	**800°C**	**850°C**	**900°C**	**950°C**
25°C	-1	0.51	0.49	0.46	0.44
150°C	-0.09	0.53	0.51	0.47	0.47
200°C	0.27	0.53	0.53	0.51	0.49
250°C	0.64	0.57	0.54	0.53	0.51
300°C	1	0.61	0.59	0.57	0.55
350°C	1.36	0.66	0.65	0.60	0.59
400°C	1.73	0.71	0.67	0.61	0.60

The first constraint equation is derived from the measured tensile strength of steel F at room temperature and these are presented in Table (4.3.18). The corresponding fitting parameters are presented in Tables A2.1(c) and A2.1(d) of Appendix A2, which leads to the mathematical expression of the fitting surface A2.Eq1(b).

Table (4.3.18): Room temperature tensile strength in MPa of steel F.

		Ultimate tensile strength (MPa) as a function of the austenitisation temperature			
Tempering temperature	**Normalised tempering temperature**	**800°C**	**850°C**	**900°C**	**950°C**
25°C	-1	1624	1934	2246	1901
150°C	-0.09	2154	2277	2375	1998
200°C	0.27	2131	2364	2280	2010
250°C	0.64	2064	2103	2054	1954
300°C	1	1982	1784	1882	1770
350°C	1.36	1710	1724	1623	1548
400°C	1.73	1687	1654	1516	1415

The second constraint is derived from the Charpy impact energy of the sub-sized specimens of steel F measured at –40°C. The results in Joules are contained in Table (4.3.19) and the fitting parameters in Tables A2.1(e) and A2.1(f) from which the regression equation may be derived.

Table (4.3.19): The Charpy impact energy at –40°C of the sub-sized specimen of steel F

		Charpy impact energy (Joules) as a function of the austenitisation temperature			
Tempering temperature	**Normalised tempering temperature**	**800°C**	**850°C**	**900°C**	**950°C**
25°C	-1	9.0	7.7	6.4	6.4
150°C	-0.09	10.3	9.0	7.7	6.4
200°C	0.27	11.5	10.3	10.3	9.0
250°C	0.64	14.1	11.5	10.3	9.0
300°C	1	16.7	12.8	11.5	10.3
350°C	1.36	17.9	15.4	12.8	10.3
400°C	1.73	17.9	16.7	15.4	14.1

The optimisation problem for steel F is written in terms of the objective function A2.1(a) and the constraint equations A2.1(b) and A2.1(c) given in Appendix 2. The fitting surfaces for steel F are graphically represented in Figure 4.3.4(a). The same scaling factors as were applied to steel E were also applied here. The optimum regions for the mechanical properties are visualised in two-dimensional plots of the iso-lines in the plane (T_{an}, T_{tn}).

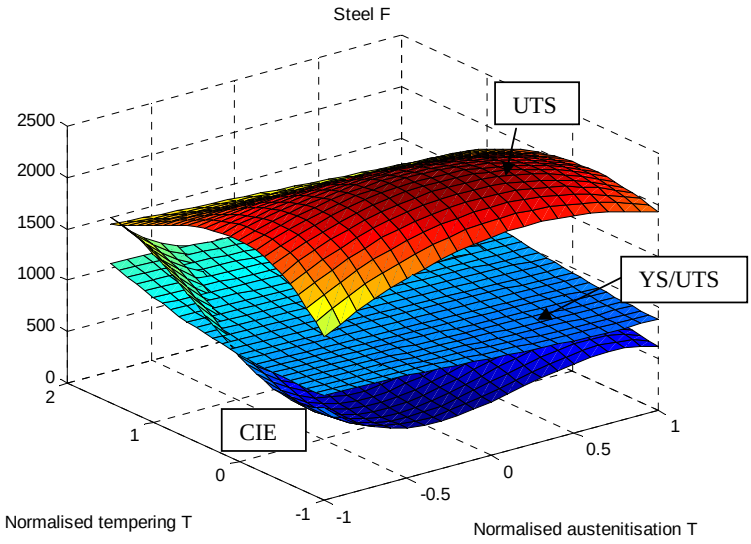

Figure 4.3.4(a): Three-dimensional representation of the optimisation problem for steel F showing the surface of the ultimate tensile strength at room temperature (upper surface), the Charpy impact energy at –40ºC (lower surface) and the objective function of the YS/UTS ratio in the middle.

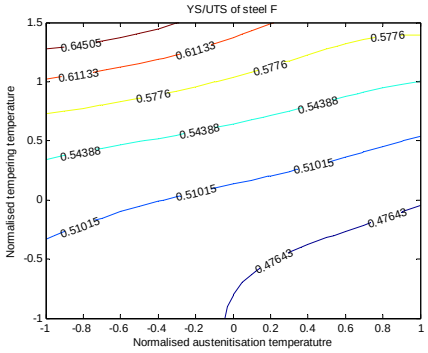

Figure 4.3.4(b): Iso-lines of the objective function YS/UTS of steel F

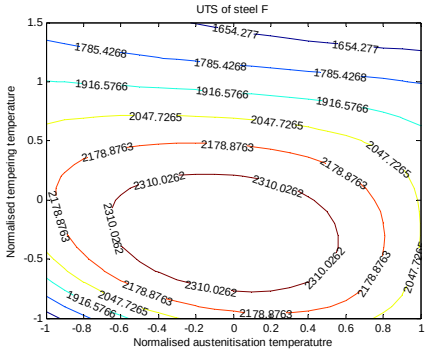

Figure 4.3.4(c): Iso-lines of the ultimate tensile strength of steel F

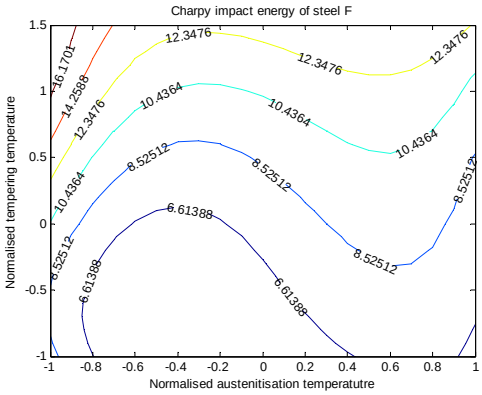

Figure 4.3.4(d): Iso-lines of the Charpy impact energy of the sub-sized specimens of steel F measured at -40°C

Figure 4.3.4(b) shows that the lower YS/UTS ratio for steel F is achieved with low normalised tempering temperatures between –1 and 0, or actually lower than 163°C. This limit is lower than the 200°C found in the case of steel E. Steels E and F have the same Carbon content of 0.39%C but have two different martensite start temperatures, which are 196°C and 255°C respectively. This difference is due to the differences in their Manganese and Chromium contents. The morphology of the martensite in these two steels is compared in section 4.4.3 through thin foil transmission electron microscopy. The tensile strength of steel F is very high compared to steel E and is also high compared to the limit specified by ARMSCOR and Mittal Steel. The tensile strength of steel F was found to be higher than 1700 MPa throughout the entire range of austenitisation and tempering temperatures used here, as shown in Figure 4.3.4(c). Steel F also has tensile elongations larger than 11% when tempered at 200°C. This steel also has the highest hardness in the as-quenched condition and also after tempering below 200°C. The Vickers hardnesses are above 720 VHN or 640 BHN. Finally it also has a higher YS/UTS ratio than steel E. More details on the comparison between these two armour steels will be given in section 4.4 after the ballistic testing and in Section (4.5) after transmission electron microscopy and atomic force microscopy.

4.3.4.3. Mechanical properties of steel G

Steel G has a lower Manganese and Chromium contents than both steels E and F. The martensite start temperature of steel G was measured as 271°C. The volume fraction of retained austenite in this steel was lower than the detection limit of the X-ray diffraction technique used in this study. The optimisation problem for steel G follows the same scheme than for steels E and F. The objective function YS/UTS ratio is derived from the results of the tensile tests at room temperature and is presented in Table (4.3.20). The similar regression analysis produced the fitting parameters in Tables A2.2(a) and A2.2(b) in Appendix 2 after which the mathematical expression of the objective function may be found.

Table (4.3.20): The yield strength to ultimate tensile strength ratio of steel G

		YS/UTS ratio as function of the austenitisation temperature			
Tempering temperature	**Normalised tempering temperature**	**800°C**	**850°C**	**900°C**	**950°C**
25°C	-1	0.66	0.61	0.49	0.46
150°C	-0.09	0.67	0.68	0.51	0.49
200°C	0.27	0.68	0.67	0.53	0.53
250°C	0.64	0.72	0.77	0.57	0.57
300°C	1	0.76	0.71	0.61	0.61
350°C	1.36	0.79	0.74	0.66	0.66
400°C	1.73	0.83	0.76	0.69	0.64

The first constraint on the system is the tensile strength and its variation with the austenitisation and tempering temperatures is presented in Table (4.3.21). The surface fitting parameters are again calculated in two steps. The first analysis produced the parameters for Equation (4.3) and the second produced the parameters for Equation (4.4). These parameters are presented in Tables A2.2(c) and A2.2(d) in Appendix 2. As may be observed, the parameters in Table A2.2(c) are some function of the austenitisation temperature. Hence they are fitted to third degree polynomials to obtain the final parameters A, B, C and D in Table A2.2(d).

Table (4.3.21). Measured tensile strength in MPa for steel G.

		Ultimate tensile strength in MPa as a function of the austenitisation temperature			
Tempering temperature	**Normalised tempering temperature**	**800°C**	**850°C**	**900°C**	**950°C**
25°C	-1	1324	1934	2120	1901
150°C	-0.09	2252	2171	2193	2089
200°C	0.27	2061	2020	1932	1926
250°C	0.63	1872	1790	1833	1750
300°C	1	1643	1631	1753	1565
350°C	1.36	1597	1594	1584	1488
400°C	1.72	1335	1326	1340	1298

The second constraint is defined by the Charpy impact energy at -40°C. The measured impact energy values in Joules, are tabulated as follows:

Table (4.3.22): Charpy impact energy in Joules measured at –40°C on sub-sized specimens of steel G

		Charpy impact energy (in Joules) as a function of the austenitisation temperature			
Tempering temperature	**Normalised tempering temperature**	**800°C**	**850°C**	**900°C**	**950°C**
25°C	-1	9.9	8.9	9.9	9.9
150°C	-0.09	17.7	14.8	16.8	13.8
200°C	0.27	18.7	15.8	16.8	15.3
250°C	0.64	18.7	16.8	17.7	15.8
300°C	1	17.7	16.8	17.7	16.3
350°C	1.36	17.7	17.3	18.2	16.8
400°C	1.73	17.7	16.3	17.7	15.8

From the results in Table (4.3.22), the fitting parameters for the Equations (4.3) and (4.4) are calculated and tabulated in Tables A2.2(e) and A2.2(f) respectively, in Appendix 2. The fitting parameters in Table A2.2(e) are again some function of the austenitisation temperature. The second regression analysis becomes necessary and gives the fitting parameters in Table A2.2(f). The second constraint of the system is written after the parameters in Table A2.2(f) and is mathematically presented in Equation A2.Eq2(c) in Appendix 2.The optimisation problem is then written in the classical form using the objective function to be minimised given by Equation A2.Eq2(a) and the two inequality constraints given by the Equations A2.Eq2(b) and A2.Eq2(c) in Appendix 2, as described in Equation (4.9). The three-dimensional representation of the system is shown in Figure 4.3.5(a). The same scaling factors applied in the two previous cases are also applied here for the same reasons. The corresponding two-dimensional representations in the (T_{an}, T_{tn}) planes are shown in Figures 4.3.5(b) through to 4.3.5(d).

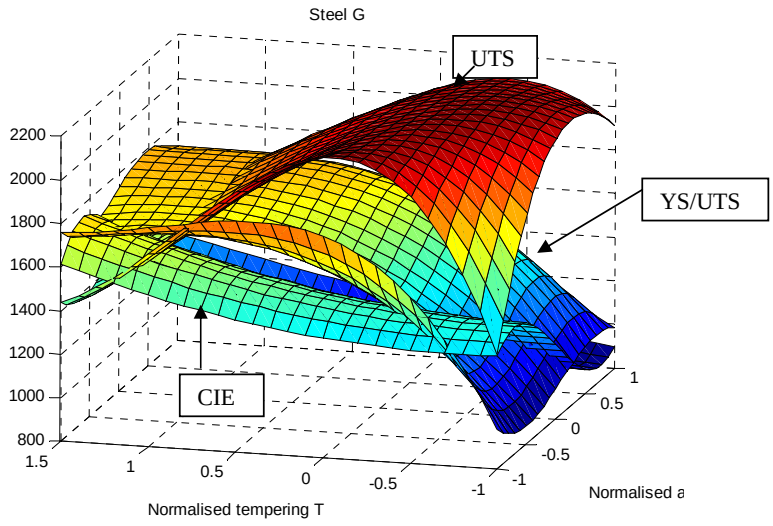

Figure 4.3.5(a): Three-dimensional representation of the objective function and the constraints in the case of steel G.

Deleted:

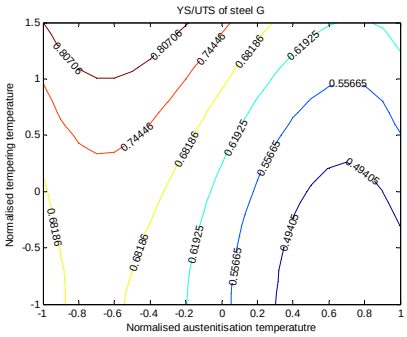

Figure 4.3.5(b): The yield strength to ultimate tensile strength ratio of the Steel G

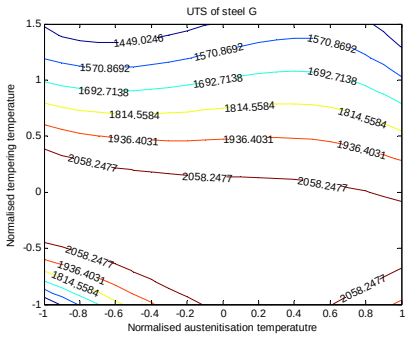

Figure 4.3.5(c): Iso-lines of the ultimate tensile strength in MPa of steel G measured at room temperature

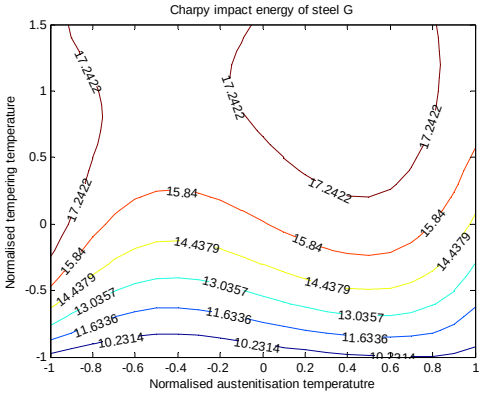

Figure 4.3.5(d): Iso-lines of the Charpy impact energy of the sub-sized specimens of steel G measured at -40°C

Some similarity of steel G to steel F may be noticed. The YS/UTS ratios are higher than in the case of steel E. The tensile strength is also higher than the specified 1700 MPa throughout the entire range of the austenitisation and tempering temperatures. The Charpy impact energy at –40°C is also higher than the specified 13 Joules throughout the entire range of the heat treatment parameters. Some resemblances are then expected between the microstructures of steel G and steel F that differ from steel E. Their martensite start temperatures are both above 250°C and no retained austenite was detected by X-ray diffraction. The ultimate tensile strength of steel G is slightly lower than for steel F but remains higher than 1700 MPa when the normalised tempering temperature does not exceed the normalised value of 1 or actually 300°C.

4.3.4.4. Mechanical properties of steel H

Steel H has the same Carbon content than steel G but has a lower martensite start temperature of 210°C, which is below 250°C. X-ray diffraction detected 4% volume fraction of retained austenite in the quenched specimens. The YS/UTS ratio of this steel as a function of the austenitisation and tempering temperatures is given in Table 4.3.23. The

regression analysis allowed the determination of the fitting parameters presented in Tables A2.3(a) and A2.3(b) in Appendix 2.

Table (4.3.23): The yield strength to ultimate tensile strength ratio of steel H

		YS/UTS ratio of steel H as a function of the austenitisation temperature			
Tempering temperature	**Normalised tempering temperature**	**800°C**	**850°C**	**900°C**	**950°C**
25°C	-1	0.46	0.44	0.44	0.43
150°C	-0.09	0.47	0.46	0.46	0.44
200°C	0.27	0.50	0.47	0.47	0.45
250°C	0.64	0.55	0.53	0.49	0.46
300°C	1	0.59	0.57	0.53	0.49
350°C	1.36	0.57	0.61	0.55	0.51
400°C	1.73	0.66	0.61	0.57	0.53

The function describing the variation of the YS/UTS ratio is noted as Equation A2.Eq3(a) in the same appendix. The constraint equation on the ultimate tensile strength is derived from the experimental measurements in Table (4.3.24) from which the fitting surface is determined. The surface fitting parameters are given Tables A2.3(c) and A2.3(d).

Table (4.3.24): The ultimate tensile strength in MPa of steel H.

		The ultimate tensile strength (in MPa) of steel H as function of the austenitisation temperature			
Tempering temperature	**Normalised tempering temperature**	**800°C**	**850°C**	**900°C**	**950°C**
25°C	-1	1415	1543	1118	822
150°C	-0.09	1905	1806	2146	1816
200°C	0.27	2020	1942	2146	1862
250°C	0.64	1902	1909	1955	1830
300°C	1	1929	1724	1894	1770
350°C	1.36	1713	1704	1698	1566
400°C	1.73	1603	1615	1678	1521

The mathematical expression of the tensile strength in MPa is written using the parameters in Table A2.3(d) and has the form given in Equation A2.Eq3(b) in Appendix 2. The second constraint is defined by the Charpy impact energy measured at -40°C and is derived from the experimental results reported in Table (4.3.25).

The surface fitting parameters obtained by regression analysis are contained in Tables A2.3(e) and A2.3(f) (Appendix 2). The equation for the Charpy impact energy surface is written in terms of the normalised temperature as Equation A2.Eq3(c). The second constraint equation is written in terms of the normalised temperatures using the parameters determined in Table A2.3(f) (Appendix 2) and is noted as Equation A2.Eq3(c).

Table (4.3.25): The Charpy impact energy in Joules of the sub-sized specimens of steel H measured at -40°C

		Charpy impact energy (in Joules) of steel H as function of the austenitisation temperature			
Tempering temperature	**Normalised tempering temperature**	**800°C**	**850°C**	**900°C**	**950°C**
25°C	-1	7.5	8	6	6.5
150°C	-0.09	19	14.5	18	12
200°C	0.27	19	15	17	14
250°C	0.64	19	13.5	17	14
300°C	1	15	10	12	11
350°C	1.36	13	8	8	8
400°C	1.73	10	7.5	8	7

The optimisation problem for the properties of steel H is stated in the classical form described in Equation (4.9) using the objective function of Equation A2.Eq3(a) and the constraint functions of Equations A2.Eq3(b) and A2.Eq3(c). The three-dimensional representation of the system is shown in Figure 4.3.6(a).

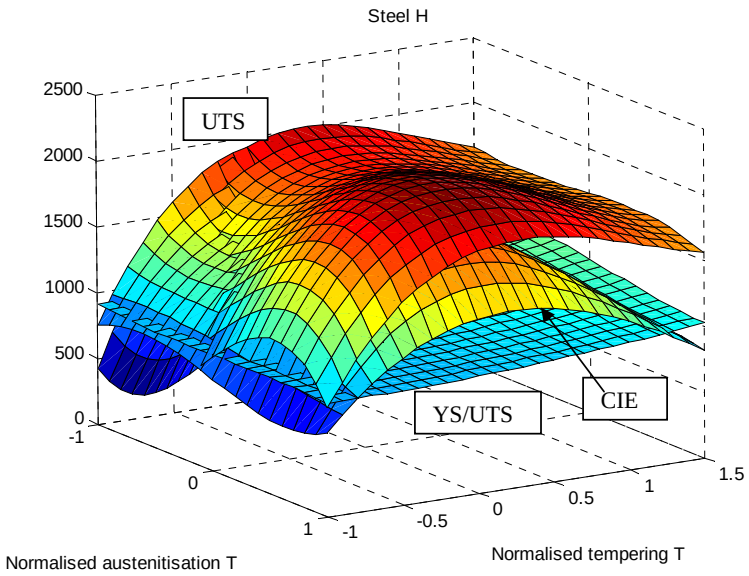

Figure 4.3.6(a): Three-dimensional representation of the optimisation problem for steel H showing the ultimate tensile strength surface(upper surface), the Charpy impact energy surface in the middle and the YS/UTS ratio in the bottom (bottom surface).

The same scaling factors than in the previous figures have been applied here. The corresponding iso-lines in the planes (T_{an}, T_{tn}) are shown in Figures 4.3.6(b) through to 4.3.6(d).

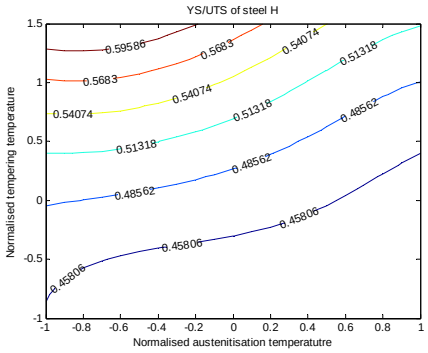

Figure 4.3.6(b): Iso-lines of the YS/UTS ratio in the plane (T_{an}, T_{tn})

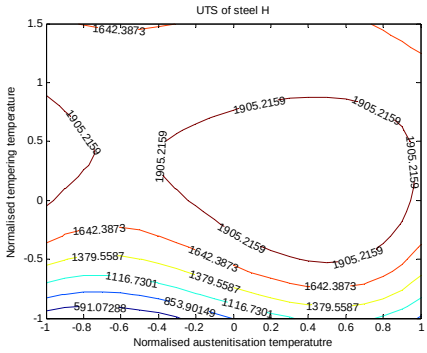

Figure 4.3.6(c): Iso-lines of the ultimate tensile strength (in MPa) of steel H in the plane (T_{an}, T_{tn})

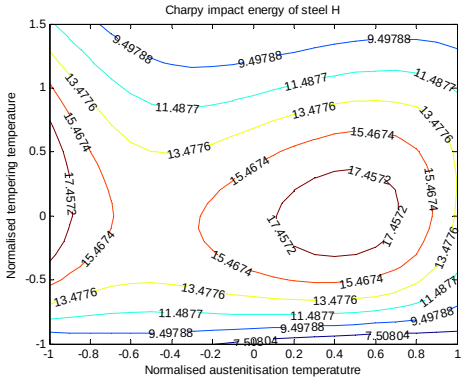

Figure 4.3.6(d): Iso-lines of the Charpy impact energy (in Joules) at –40°C of steel H

Steel H has intermediate values of the YS/UTS ratio, lying between steel E on one side and steels F and G on the other side. Like steel E it presents a brittle behaviour in the untempered condition, where it is difficult to measure the ultimate tensile strength. The tensile strength of this steel has also intermediate values between the two groups of steels previously identified. It remains close and above the specified 1700 MPa after tempering at 350°C for the entire range of the austenitisation temperature. The Vickers hardness of steel H also remains above 550 VHN after tempering at 300°C for one hour. The resistance to tempering of this steel is due to its high Silicon content. It is well known that Silicon delays the transformation of the transition ε - carbide to cementite during tempering.

4.3.4.5. Mechanical properties of steel I

The martensite start temperature of steel I measured by dilatometry was found to be 309°C, which is higher than the martensite temperatures of the other four steels. The volume fraction of retained austenite in the quenched condition was lower than the detection limit of the X-ray diffraction technique used for the analysis. The results of the measurement of the YS/UTS ratio of this steel are shown in Table (4.3.26). It may be observed that steel I

presents the highest values of the YS/UTS ratio of all of the five steels considered up to here.
The YS/UTS ratio of steel I in the quenched condition is in the same range than that of steels E and H after low-temperature tempering. The relatively high values of this ratio for steel I may be caused by auto-tempering during the quenching of this steel, in view of its relatively high M_s temperature.

Table (4.3.26): The YS/UTS ratio of steel I

		YS/UTS ratio as a function of the austenitisation temperature			
Tempering temperature	**Normalised tempering temperature**	**800°C**	**850°C**	**900°C**	**950°C**
25°C	-1	0.66	0.62	0.6	0.62
150°C	-0.09	0.70	0.71	0.61	0.61
200°C	0.27	0.74	0.74	0.63	0.63
250°C	0.64	0.78	0.74	0.63	0.62
300°C	1	0.80	0.78	0.64	0.64
350°C	1.36	0.83	0.77	0.66	0.64
400°C	1.73	0.83	0.81	0.71	0.66

The objective function describing the YS/UTS ratio is written in terms of the normalised temperature using the fitting parameters in Table A2.4(b) in Appendix 2 and is noted as Equation A2.Eq4(a). The constraints on the system are derived from the results of the tensile tests and the Charpy impact tests. Table (4.3.27) contains the results of the ultimate tensile strength measurements. The fitting parameters for the ultimate tensile strength surface of this steel are presented in Tables A2.4(c) and A2.4(d) of Appendix 2.

Table (4.3.27): The ultimate tensile strength (in MPa) of steel I

		Ultimate tensile strength (in MPa) as a function of the austenitisation temperature			
Tempering temperature	**Normalised tempering temperature**	**800°C**	**850°C**	**900°C**	**950°C**
25°C	-1	2100	1954	1948	1543
150°C	-0.09	2040	1920	1900	1755
200°C	0.27	1842	1751	1763	1649
250°C	0.64	1714	1675	1623	1588
300°C	1	1515	1446	1485	1452
350°C	1.36	1447	1453	1434	1327
400°C	1.73	1312	1261	1284	1187

The mathematical equation describing the tensile strength of steel I is then derived from the parameters in Table A2.4(d) (Appendix 2) and noted as Equation A2.Eq4(b). The second constraint is derived from the measured vales of the Charpy impact energy at -40°C using the experimental values in Table 4.3.28.

Table (4.3.28): Charpy impact energy of the sub-sized specimens of steel I at -40°C

		Charpy impact energy as a function of the austenitisation temperature			
Tempering temperature	**Normalised tempering temperature**	**800°C**	**850°C**	**900°C**	**950°C**
Ally 25°C	-1	16	17	17	17
150°C	-0.09	18	19	19	19
200°C	0.27	19	19	20	20
250°C	0.64	18	19	20	19
300°C	1	18	19	19	20
350°C	1.36	19	19	19	21
400°C	1.73	18	20	20	21

The equation representing the Charpy impact energy of the sub-sized specimens of steel I measured at -40°C, is finally derived from the parameters contained in Table A2.4(f) and noted as Equation A2.Eq4(c). The optimisation problem is stated in classical form by substituting the objective function in Equation A2.Eq4(a) and the constraint functions in Equations A2.Eq4(b) and A2.Eq4(c) in the system defined in Equation (4.9). The three-dimensional representation of this system, using the previous chosen scaling factors, is presented in Figure 4.3.7(a).

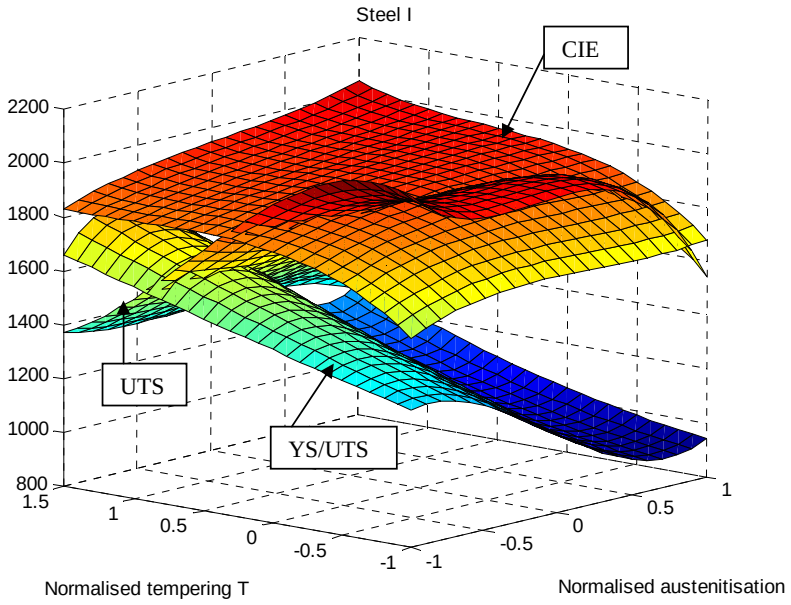

Figure 4.3.7(a): Three-dimensional representation of the optimisation system for steel I.

From Figure 4.3.7(a), it may be observed that the surface representing the Charpy impact energy of steel I is at high levels and it remains high throughout the entire range of heat treatment parameters considered.

However the ultimate tensile strength surface drops to levels lower than 1700 MPa when the tempering temperature is higher than 200°C. The corresponding iso-lines are shown in Figures 4.3.7(b) through to 4.3.7(d).

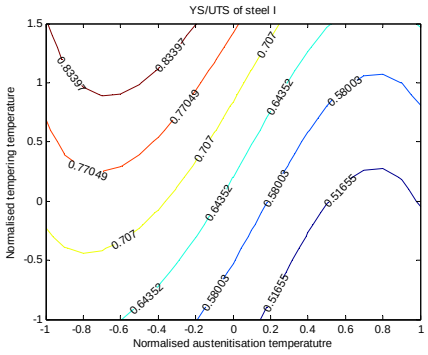

Figure 4.3.7(b): Iso-lines of the yield strength to ultimate tensile strength ratio of steel I

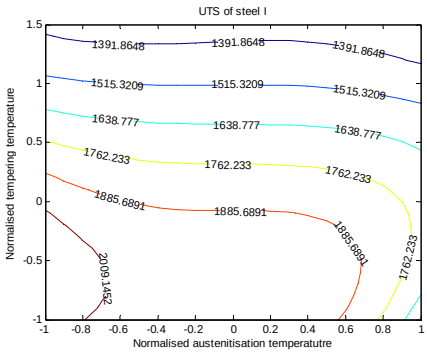

Figure 4.3.7(c): Iso-lines of the tensile strength of steel I.

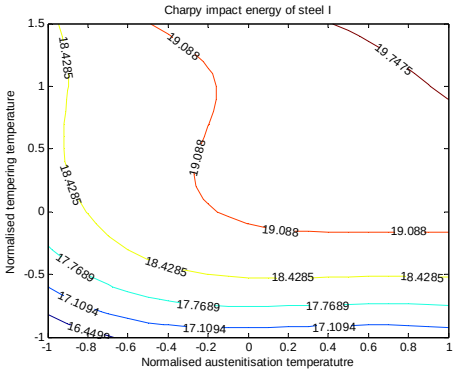

Figure 4.3.7(d): Iso-lines of the Charpy impact energy of steel I measured at -40°C

4.3.5. General observations on the mechanical properties of steels E through to I.

From the results of the measurements presented in Section 4.3.4, it appears that the five armour steels considered may be classified following their martensite start temperatures. Three groups of armour steels may be defined. The first group of armour steels, comprising steel E and steel H, have relatively low martensite start temperatures, lower than 210°C. The second group comprises steels F and G which has martensite start temperatures near to 250°C. The third group comprises steel I which has martensite start temperatures near to 300°C. The YS/UTS ratios of these steels are plotted for graphical comparison in Figure 4.3.8.

Table (4.3.29). Groups of armour steels classified according to the martensite start temperatures for the austenitisation temperatures comprised in the range from 800°C to 950°C.

Group	Armour steel	Martensite start temperature	YS/UTS
1	E	196°C	< 0.6
	H	210°C	
2	F	255°C	0.65 to 0.75
	G	271°C	
3	I	309°C	> 0.70

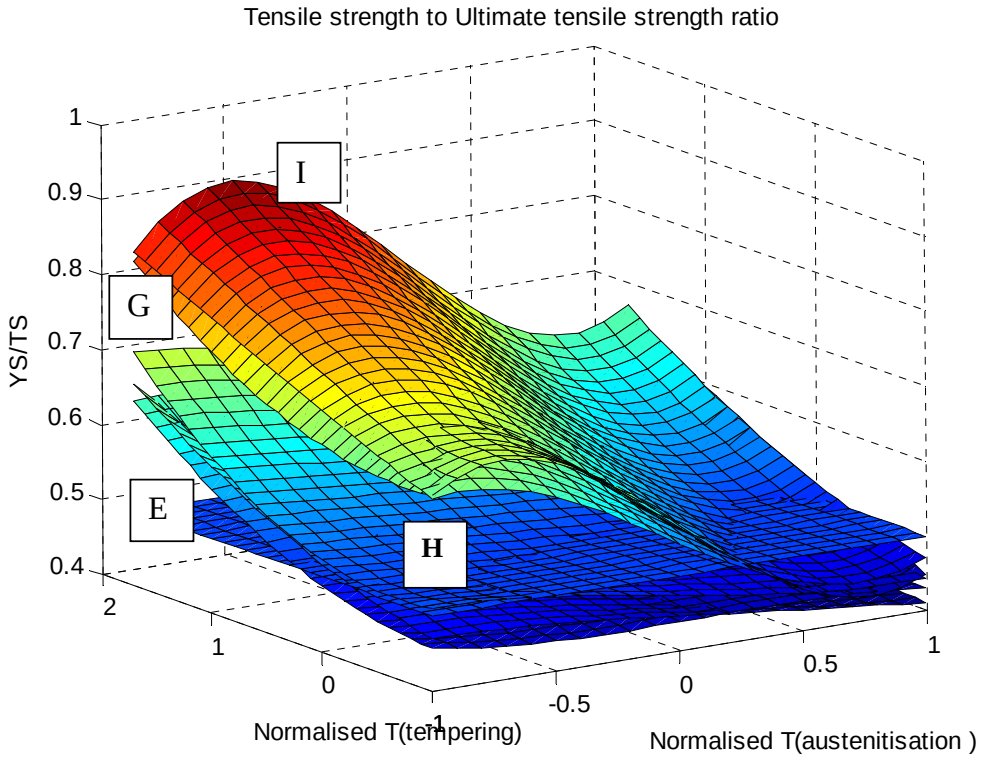

Figure 4.3.8: Showing the comparison of the levels of the yield strength to ultimate tensile strength ratio surfaces of the steels E through to I. Steel I and steel G on top, steel E, steel F and steel H on the bottom. The plane of YS/UTS=0.5 is also shown.

From this figure it may be observed that high martensite start temperatures lead to high values of the YS/UTS ratio in the quenched as well as in the tempered conditions for these five armour steels. The YS/UTS ratio increases with an increase in the tempering temperature. The high values of this ratio in the cases of high martensite temperatures, is probably a consequence of auto-tempering during quenching. However, this ratio decreases with an increase in the austenitisation temperature which leads to grain growth and an increase in the volume fraction of retained austenite because of the lower martensite start temperature. The volume fraction of retained austenite in the armour steels becomes the main factor determining the YS/UTS ratio. This ratio is lower in the conditions corresponding to a higher volume fraction of retained austenite in these armour steels. This is the case for the two armour steels E and H in the first class.

The tensile strength of steel E (group 1) and steel F (group 2) are compared in Figure 4.3.9, where the plane of 1700 MPa is also shown. The gap in the tensile strength between these two groups of armour steels is large. It was noted earlier that the steels A (M_s =285°C), B (M_S = 253°C), C (M_S =241°C) and D (M_S =265°C) are currently in production by Mittal Steel and others and are already utilised in military and security applications. The

specifications for these ballistic purposes are stated in terms of the yield strength that should be higher than 1500 MPa and the tensile strength, that should be higher than 1700 MPa. These two strength limits will lead to values of the YS/UTS ratio close to 0.88 and will lead to the occurrence of localised yielding during impact. Experience within the industry has found that steel C has a better ballistic performance than the other three for plate thickness between 8.5 mm up to 30 mm. In the current assessment methodology, steel A, steel B and steel D may, therefore, be classified into the second class, whereas steel C belongs to the transition between the first class and the group 2 of armour steels as previously defined from their martensite start temperatures.

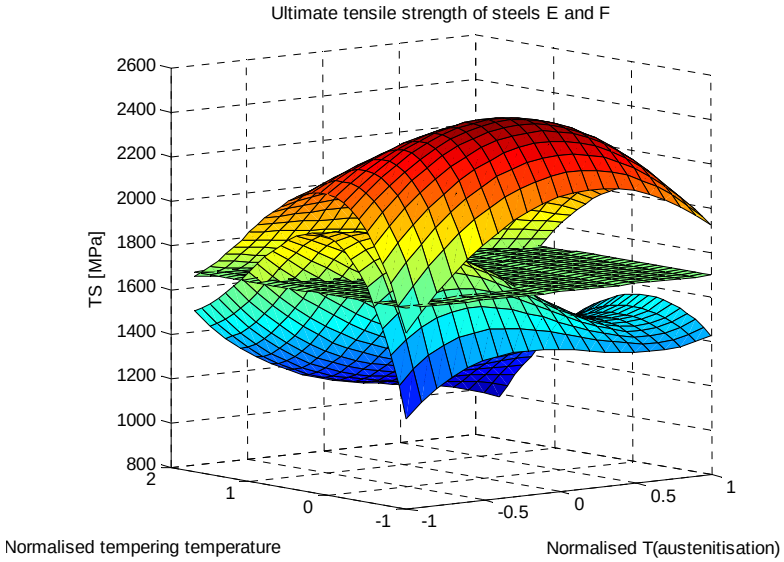

Figure 4.3.9: Comparison of the ultimate tensile strength between steel E (group 1) in the lower surface, steel F (group 2) in the upper surface and the specified plane of 1700 MPa.

The armour steels in group 3 (high martensite start temperatures) have an intermediate tensile strength between those in the first and in the second groups. The same observation is valid for their hardnesses. Hence the second group of armour steels is currently produced for military applications based on the design philosophy that would link the ballistic performance to the hardness and the tensile strength of these steels. Earlier in Chapter 2 mention was made of a new approach in the definition of the Ballistic Performance Index where the hardness of the armour steel is no longer an important determinant. Rather the tensile strength is considered to be important as it compares well to the true fracture strength during high-velocity impact. In the present study the YS/UTS ratio is also considered in predicting the ballistic performance of the armour steels and comparison is made between the three modes of predicting the ballistic performances using (i) the hardness of the plates, (ii) their ballistic performance index BPI, or (iii) their YS/UTS ratio.

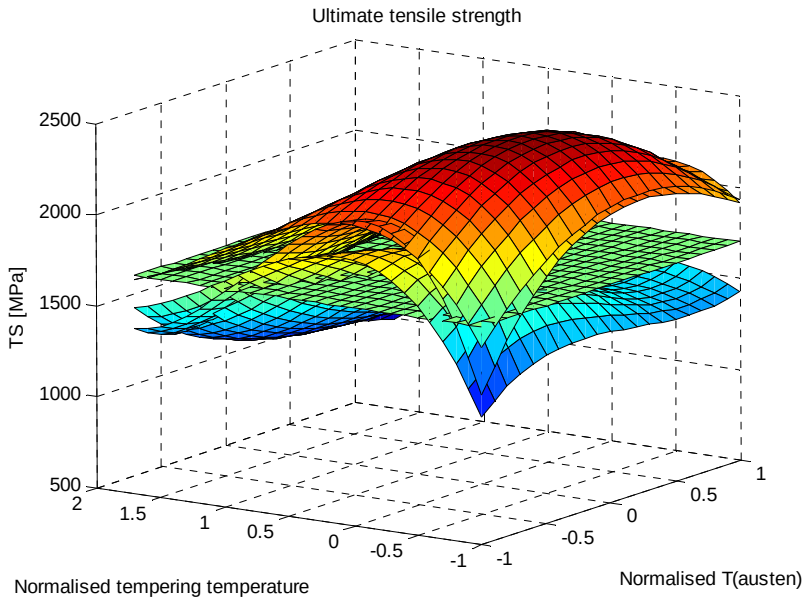

Figure 4.3.20: Comparison between the tensile strength of steels E, F and I showing the intermediate level of the strength of steel I (group 3) between that of steel F (group 2) in the upper surface and steel E (group 1) in the lower surface. The plane of 1700 MPa is also shown.

The Charpy impact energy at -40°C of steels E, F, G and I are compared in Figure 4.3.21, where it may be observed that steel I (group 3) has the highest impact energy (upper surface) throughout the entire range of the austenitisation and tempering temperatures, whereas steel E and steel H (group 1) have the lowest impact energy (lower surfaces) throughout the entire range of the austenitisation and tempering temperatures considered in this study. Steel F (group 2) has a fairly intermediate level of Charpy impact energy. It also appears from Figure 4.21 that the Charpy impact energy of the sub-sized specimens of the armour steels measured at –40°C, increases when the martensite start temperature of the armour steel is higher.

The fracture surfaces after the tensile tests at room temperature and the Charpy impact tests at -40°C of these three classes of armour steels, as classified according to their martensite temperatures, are compared in Section 4.3.6. The effect of Silicon, Chromium and Manganese contents in their resistance to low-temperature tempering, are also analysed. The effect of the shape and the size of the Manganese sulphide particles on the fracture mode of these armour steels is particularly examined.

4.3.6. Fracture analysis after the Charpy impact and the tensile tests.

4.3.6.1. Group 1 armour steels

The fractured surfaces of the Charpy specimens of steels E (0.003%S, 1.22%Mn) and H (0.011%S, 1.15%Mn) whose martensite start temperatures are respectively 196°C and 210°C, were analysed by secondary electron scanning electron microscopy. Two areas were considered in each fractured surface, firstly, where only the shear lips were analysed

for the sake of the mechanism by which the fracture was initialised, and secondly, the unstable propagation of the crack that occurred throughout the cross-section of the specimen.

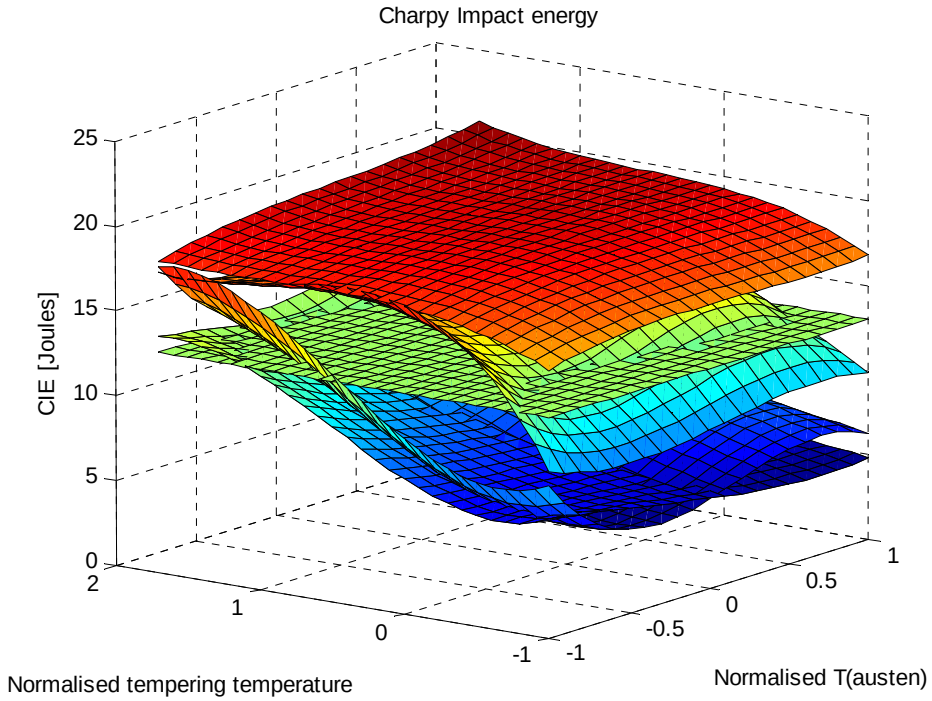

Figure 4.3.21. Comparison between the Charpy impact energy of the sub-sized specimens of steel E (lower surface), steel H (second lower surface), steel G (second upper surface) and steel I (upper surface). The plane of the specified 13 Joules is also shown.

The first area was generally near the standard notch of the Charpy specimen while the second area was situated within the fracture face at a position below the notch and very near to the area of contact with the striking edge of the pendulum. The Charpy impact energy of the sub-sized specimens, measured at -40°C, allowed the selection of the three tempering temperatures for steel H, as shown in Figure 4.3.22. The Charpy impact energy of these two steels remains lower than the specified 13 Joules in the untempered condition and also when tempered at temperatures lower than 200°C. It exceeds 13 Joules, however, when the steels E and H are tempered at temperatures between 200 and 300°C and decreases again when the tempering temperature is higher than 300°C. The untempered Charpy specimens and those tempered at 200°C and at 300°C for 20 minutes and for 60 minutes, were selected for observation in the scanning electron microscope.

From Figure 4.3.22 it appears that the armour plates in the group 1 (low martensite start temperatures) fractured by a brittle inter-granular mechanism in the untempered condition during the test at -40°C. The former austenite grain size is the operating grain size during the fracture. This behaviour is more noticeable in the shear lips formed near to the notch in the specimens (Figure 4.3.22(a-1)) than in the shear lips near the impact point

(Figure 4.3.22(a-2)) where fracture rather occurs by a compound mechanism involving an inter-granular and a trans-granular mechanism. The specimens tempered at 200°C again show a more brittle behaviour near to the notch (Figure 4.3.22(b-1)) than near to the impact point (Figure 4.3.22(b-)2). Tempering at 200°C slightly improved the toughness of these armour steels and increased their Charpy impact energy to 12 Joules. Dimples were formed in areas near the faces close to the impact area away from the notch. At the same time the effect of Manganese sulphide particles becomes observable (craters on the bottom of Figure 4.3.22(b-2)). Tempering at 250°C led to values of the impact energy between 13 Joules and 18 Joules for steels E and H. The fracture of these Charpy specimens became ductile with small dimples formed near the notch (Figure 4.3.22(c-1)) as well as near the impact area away from notch. The size of the plastically deformed regions around the Manganese sulphide particles became larger as may be observed in the Figure 4.3.22(c-2). The decrease in the Charpy impact energy of the specimens upon tempering above 300°C is partially attributed to the detrimental effect of the Manganese sulphide particles in a relatively soft martensite when the tempering temperature exceeds 200°C.

The brittle inter-granular fracture near the notch of the Charpy specimens may be explained by the stress concentration effect of the notch that introduces local stresses higher than the nominal stress far from the notch during the impact test.

Tempering produces carbides and removes the Carbon from solid solution in the martensite and it is this that lowers the hardness and increases the toughness. However the detrimental effect of the Manganese sulphide particles plays a role in the fracture mechanism of these steels and imposes a limit to their increase in toughness with fracture cavities of up to 7 μm that were formed. The shape of the Manganese sulphide particles has a strong effect on the stress concentration effect during impact and tensile loading as will be shown later in this paragraph. The shape is important but of equal importance here is the very low adhesion between the ferrite matrix and MnS particles. Specifically, upon tempering above 250°C the softening of the martensite promotes the decohesion around the elongated Manganese sulphide particles. Cavities of diameters larger than 16 μm were formed upon unstable shearing of the areas around the Manganese sulphide particles as illustrated in Figure 4.3.22(c-2). The Charpy impact energy of these armour steels becomes once again lower upon tempering at 400°C.

Backscattered scanning electron microscopy of the untempered and the specimen tempered at 400°C for 60 minutes, show the advanced decomposition of the martensite into ferrite and cementite in between the plates previously formed upon quenching. A high magnification is necessary to observe this advanced decomposition of the martensite as shown in Figures 4.3.23(a-1) to 4.3.23(b-2). At a low magnification of about 1700X the shape of the martensite plates seems unaltered upon tempering at 400°C (Figure 4.3.23(b-1)) compared to the untempered condition (Figure 4.3.23(a-1)). But a higher magnification of about 20000X reveals the decomposition of the martensite whereas in the untempered condition backscattered electron microscopy does not reveal the presence of any cementite (Figure4.3.23(a-2)).

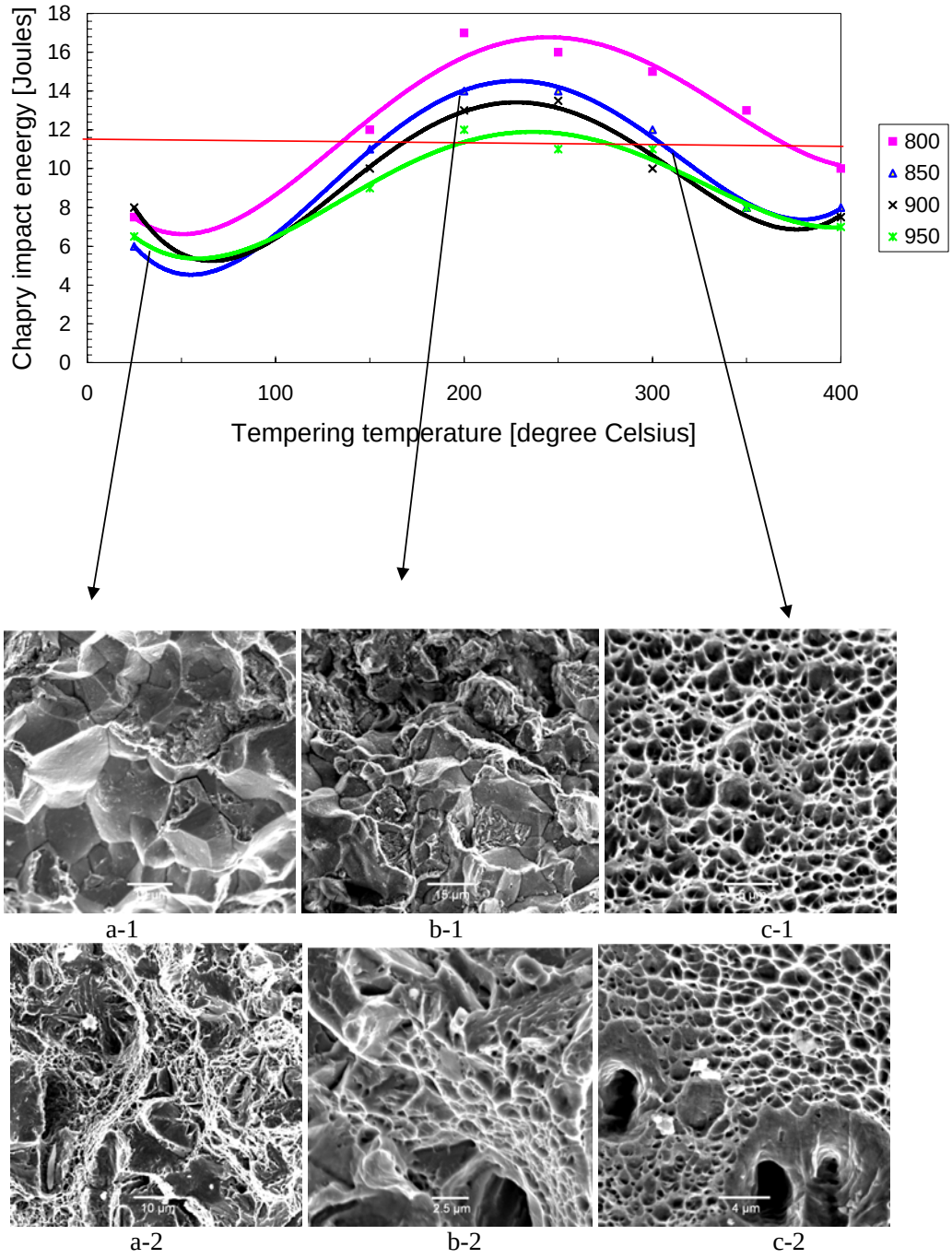

Figure 4.3.22. Secondary electron scanning electron micrographs of the fractured Charpy specimens of steel H after testing at -40°C, showing the evolution of the operating mode during the fracture as a function of the tempering temperature and the effect of the notch.

Fig. 4.3.22(a-1) and (a-2): SEM fractograph of steel H austenitised at $850^{0}C$, quenched in water showing a brittle inter-granular fracture near the notch (Figure a-1), and a quasi cleavage fracture near the incidence site of the specimen in direct contact with the striking edge of the pendulum.

Fig. 4.3.22(b-1) and (b-2): SEM fractograph of steel H austenitised at $850^{0}C$, quenched in water and tempered at $200^{0}C$, showing brittle fracture near to the notch and a more ductile fracture near the impact area away from the notch. Cavities were formed around the MnS particles.

Fig. 4.3.22(c-1) and (c-2): SEM fractograph of steel H austenitised at $850^{0}C$, quenched in water and tempered at $300^{0}C$, showing ductile fracture near the notch as well as near the impact area away from the notch. Small equi-axed dimples and large cavities had formed around the MnS particles.

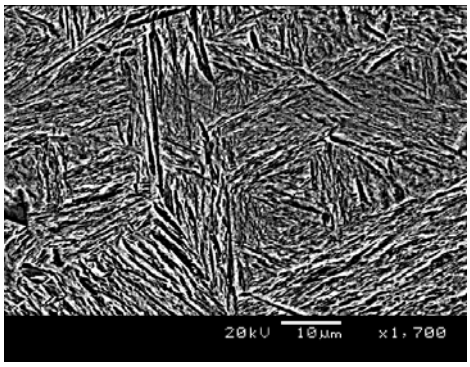

Figure 4.3.23(a-1): SEM of untempered and polished sample of the steel H at 1700 magnification

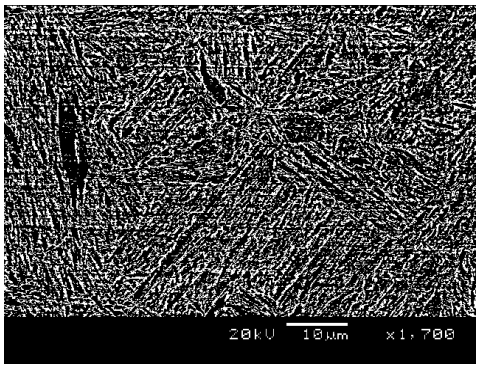

Figure 4.3.23(b-1): SEM of polished sample of steel H tempered at 400°C (×1700 magnification)

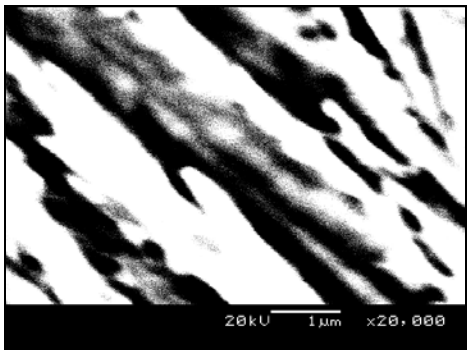

Figure 4.3.23(a-2): SEM of untempered and polished sample of steel H at 20000 magnification

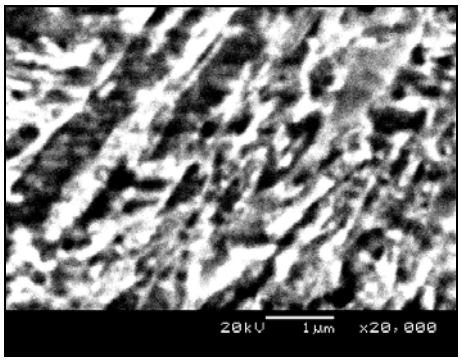

Figure 4.3.23(b-2): SEM of polished sample of steel H tempered at 400°C (×20000 magnification)

The presence of the cementite and the Manganese sulphide is, therefore, prejudicial to the resistance against impact loading despite the presence of the soft ferrite. The shear lips of the tensile specimens have also been examined in secondary electron scanning electron microscopy. The brittle behaviour of the armour steels in the untempered condition makes it very difficult for the determination of the tensile properties. Figure 4.3.24 shows the fracture surface under tensile stress of steel H in the quenched and untempered condition. It confirms that the brittle behaviour in the case of a low strain rate axial loading is less severe than one under impact loading as was illustrated in the Figures 4.3.22(a-1) and

4.3.22(a-2). The fracture surface of the untempered tensile specimens presents features of brittle fracture by decohesion of the grains as can be seen in Figure 4.3.24. Cavities of 2.5 μm are formed around the spherical inclusions of Manganese sulphide. The elongated plate-like inclusions of Manganese sulphide increases the size of the cavities to more than 12 μm that are formed during the tensile test and are shown in Figure 4.3.25 . This phenomenon may by explained by the occurrence of localised high stresses around the inclusions of the Manganese sulphide plates and consequently it leads to a decrease of the nominal ultimate tensile strength of the armour steel upon tempering. The other reason for this decrease of the ultimate strength is the decomposition of the martensite itself and the formation of coarse cementite.

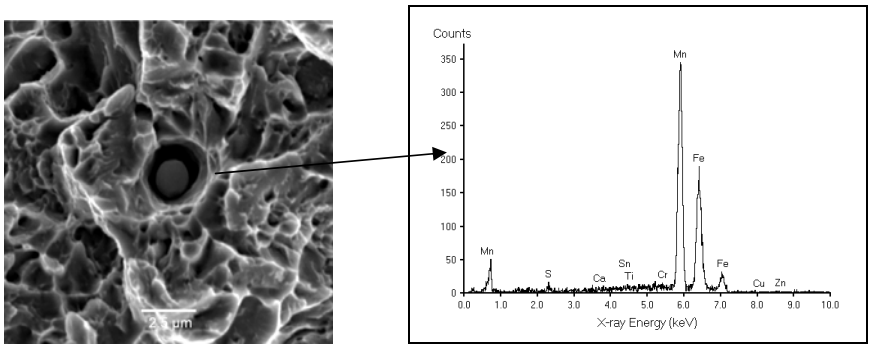

Figure 4.3.24: Secondary electron scanning microscopy of the shear lips of steel H in the quenched and untempered condition, showing spherical inclusions of MnS after tensile test.

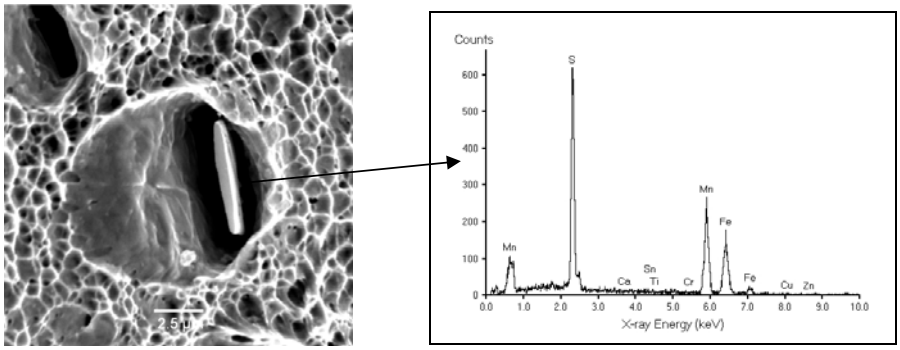

Figure 4.3.25: An elongated plate-like inclusion of Manganese sulphide, observed after the tensile test of steel H tempered at $150\,^{0}C$, showing large cavities around the inclusions of the MnS.

4.3.6.2 Group 2 armour steels

The sub-sized Charpy specimens of steel F (0.009%S, 0.65%Mn) whose martensite start temperature is 255°C, have shown the same brittle behaviour in the untempered condition as was the case with the steels E and H but with a slightly higher impact energy. Besides the mentioned reasons of the brittle behaviour in the untempered condition, other inclusions such as the Calcium-Aluminium compounds inherited from the casting process also act as stress raisers and, therefore, act as crack initiators in the hard untempered martensite during the tensile test. The initiation of such cracks is illustrated in Figure 4.3.26. For steel F also

the effect of the Manganese sulphide inclusions becomes observable and large cavities were formed around this type of inclusion that weakens the armour steel when the tensile or the Charpy specimens are tempered at temperatures above 200°C, as illustrated in Figure 4.3.27.

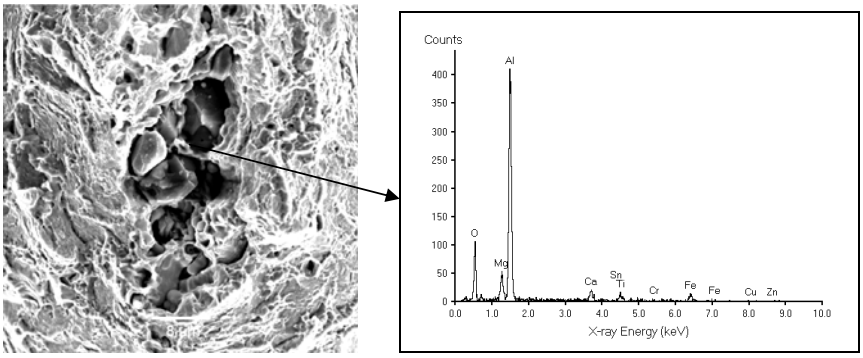

Figure 4.3.26: Crack initiation near an inclusion of a Calcium-Aluminium-Oxygen compound in the tensile specimen of steel F.

The comparison between the fracture appearances of the shear lips in the untempered and the tempered conditions in steel F also showed a transition from brittle to ductile fracture when the specimens were tempered at 200°C.

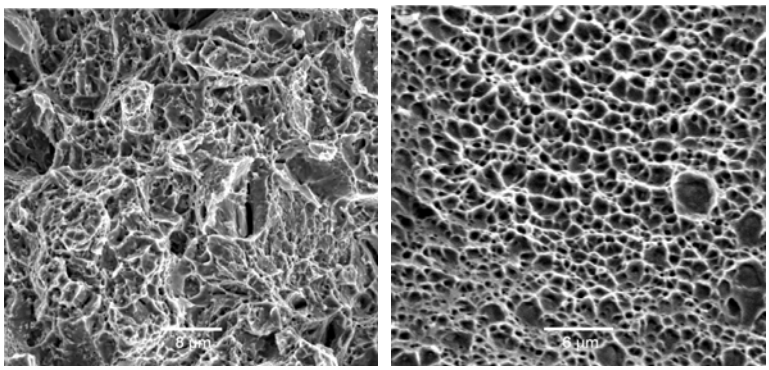

Fig. 27(a) Fig. 27(b)

Fig 4.3.27. Secondary electron scanning microscopy of Steel F after tensile testing at room temperature (a) austenitised at 900^0C and water quenched, (b) austenitised at 900^0C, water quenched and tempered at 200^0C, showing dimples that indicate ductile fracture during the tensile test.

The mechanical properties of steel F in the above mentioned conditions are shown in Table (4.3.30).

Table (4.3.30): Mechanical properties of the steel F austenitised at 900°C for 1 hr, in the quenched condition and after tempering at 200°C.

	UTS [MPa]	Elongation A_f %	Impact energy at -40 ^0C [J]
Austenitised and quenched	2246	4	7
Austenitised, quenched and tempered at 200°C	2280	9	12

The ultimate tensile strength and the elongation of steel F (M_S = 255°C), containing 0.6% volume fraction of retained austenite is very high compared to that of steels E (M_S = 196°C, 5% retained austenite) and H (M_S = 210°C, 4% retained austenite) in the same conditions. The impact energy of steels F and H are comparable. It has been mentioned previously that the tensile properties were very difficult to determine in the untempered condition in the case of steels E and H because of their brittle behaviour. The intermediate martensite start temperature of the Group 2 armour steels led to the highest ultimate tensile strength and hardness but it did not improve the impact energy compared to the armour steels of Group 1.

4.3.6.3. Group 3 armour steels

The fracture of steel I (0.012%S, 0.39%Mn) whose martensite start temperature was 309°C, was ductile with formation of dimples within the grains under tensile stress, as shown in Figure 4.3.28. The auto-tempering of the martensite laths increases the elongation to fracture to 11% of this armour steel. The same goes for the impact energy that supersedes 16 Joules in all the conditions. On the other hand, the ultimate tensile strength decreases from 2000 MPa to values below 1300 MPa due to the auto-tempering and the tempering effects.

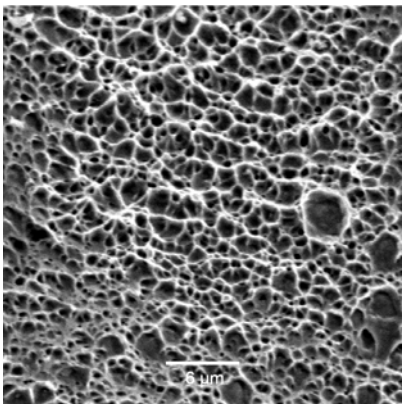

Figure 4.3.28: Typical surface fracture appearance of steel I under tensile stress austenitised 30 min at 850°C and tempered at 150°C for 1 hr

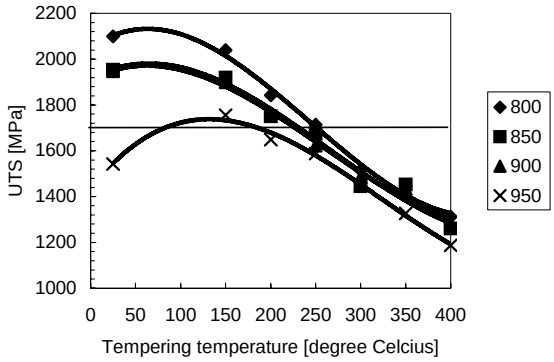

Figure 4.3.29: Ultimate tensile strength of steel F. austenitised for 30 min at the given temperatures and tempered for 1 hr.

4.3.6.4 General observations

The surface appearance of the fractured faces after the tensile and impact testing showed significant differences between the specimens that produced higher and those that produced lower mechanical properties, as observed in secondary electron scanning electron microscopy. The surface appearances were analysed on the shear lips where the fracture initiated before the unstable propagation of the cracks through the cross section.

The brittle fracture of steels E and H indicates that they cannot be used in the untempered condition because of the risk of spallation if impacted by high velocity projectiles. The tempering treatment at temperatures ranging between 150°C and 250°C has increased the ability of the armour steels of Group 1 and 2 to undergo ductile plastic deformation at room temperature and at sub-zero temperatures. The secondary electron scanning electron microscopy also showed that the tempering treatment enhanced the negative effect of the Manganese sulphide particles. Inclusions of Manganese sulphide were not observed in steel E that contains only 0.003% Sulphur. The notch in Charpy testing enhanced the brittle behaviour and inter-granular fracture of the untempered armour steels in Group 1. All potential stress raisers should therefore be avoided in the manufacturing of armour plates.

Any inclusions have negative effects on both the strength and the resistance to impact loading. Other workers [71] have observed the influence of the shape, the distribution and the size of the Manganese sulphide particles on the strength of steels. In this study two types of inclusions, namely Manganese sulphide and the Calcium-Aluminium-Oxygen compounds have been identified in the fractured surfaces.

The tensile strength, the elongation and the resistance to impact loading may then be improved by developing cleaner steels without Sulphur and inclusions or by lowering the volume fraction of the Manganese sulphide. For improving the toughness of these steels, it is then suggested that the control of Manganese sulphide shape and size in the as-cast condition be introduced with the goal of equi-axed sulphide particles of the largest possible size to increase their interspacing throughout the matrix. A small interspacing between the Manganese sulphide inclusions will be negative as illustrated in Figure 4.3.30.
The most useful compositions should be those, which promote equi-axed sulphide particles (Type III). Type III sulphides are faceted equi-axed particles and are favoured by low oxygen levels in combination with high Carbon levels, and are promoted by Silicon and Aluminium additions. There is also an effect of Sulphur content on sulphide type, with type III sulphides favoured as the sulphur content is reduced.

The cooling rate upon solidification can also influence the sulphide type. Type II sulphides (rosette-like or fan-like) are favoured over both Type I (spherical) and type III sulphides as the cooling rate is increased.

The second type of inclusions seen in these fractured surfaces, are the coarse particles of a Calcium-Aluminium-Oxygen compound inherited from the steel-making process. Secondary electron scanning electron microscopy has shown that micro-cracks within the hard martensitic armour steel, are initiated near and around these type of inclusions before they propagate toward the surface of the tensile specimen. Therefore, they act as stress raisers and participate in the reduction of the nominal tensile strength of the armour steels.

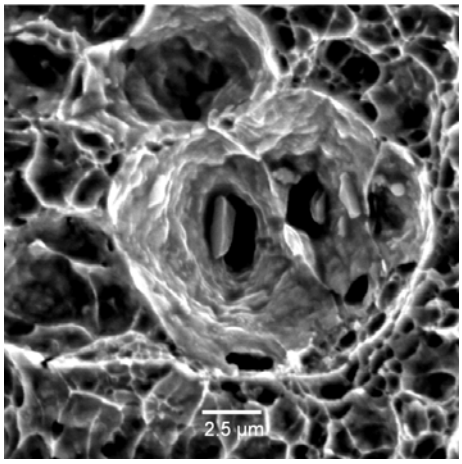

Figure 4.3.30: Effect of the small interspacing between inclusions of MnS in steel F

4.3.7. Martensite start temperatures of the armour steels.

Measurements of the martensite start temperatures of steels E through to W whose chemical compositions are given in Tables 4.3.31 and 4.3.32, were done using dilatometry. The measured values have been compared to values calculated using two different formulas published in the literature. The scatter between the measured and the calculated values using these two formulas have suggested the determination of another multi-linear approximation for the prediction of the martensite start temperatures for these armour steels.

The main hypothesis made for this estimate is the dependence of the M_S temperature on the chemical composition. The predicted values of the martensite start temperature were calculated from the following formulas:

- After Stevens and Haynes [73] based on 59 steels without considering any interaction parameters between alloying elements themselves:

$$M_s\left({}^0C\right) = 539 - 423C - 30.4Mn - 17.7Ni - 12.1Cr - 7.5Mo - 7.5Si + 10Co \quad (4.12)$$

- After Wang et al [73] based on 157 steels and considering interaction parameters between alloying elements using an Artificial Neural Network analysis (ANN):

$$\begin{aligned} M_s\left({}^0C\right) = {} & 540 - 584\,W_C - 23.1W_{Si} - 117.7W_{Mn} - 42.5W_{Cr} - 49\,W_{Mo} - 62.5W_{C-Si} + \\ & 178.3W_{C-Mn} - 10.0_{C-Cr} + 52.5W_{C-Mo} + 117.2W_{Si-Mn} + 50.9W_{Si-Cr} - 142.2W_{Si-Mo} - \\ & 129.2W_{Mn-Cr} - 9.7W_{Mn-Mo} + 69.9W_{Cr-Mo} \end{aligned} \quad (4.13)$$

Table (4.3.31): Chemical composition (wt%) of the steels tested for the development of advanced performance steel armour plates

	C	Mn	P	S	Si	Cu	Ni	Cr	Mo	V	Nb	Ti	N
Steel E	0.39	1.22	0.008	0.003	0.21	0.102	2.99	1.49	0.5	0.006	0.002	0.003	0.0049
Steel F	0.39	0.65	0.017	0.009	0.8	0.23	2.8	0.22	0.24	0.003	0.006	0.01	0.0051
Steel G	0.37	0.40	0.016	0.011	0.43	0.33	2.3	0.24	0.3	0.006	0.006	0.009	
Steel H	0.37	1.15	0.015	0.011	1.06	0.14	3.8	0.52	0.43	0.008	0.008	0.007	0.0036
Steel I	0.34	0.39	0.019	0.012	0.40	0.32	2.43	0.27	0.37	0.009	0.009	0.008	
Steel J	0.30	0.48	0.018	0.012	0.35	0.12	1.4	0.48	0.19	0.01	0.01	0.015	0.0059
Steel K	0.3	0.65	0.016	0.017	0.75	0.11	2.83	0.84	0.45	0.01	0.01	0.01	
Steel L	0.30	0.97	0.018	0.013	0.93	0.12	4.1	0.83	0.69	0.005	0.008	0.012	
Steel M	0.43	1.21	0.018	0.012	0.76	0.13	4.34	1.52	0.44	0.005	0.01	0.01	0.0049
Steel N	0.42	0.63	0.016	0.014	0.5	0.11	2.8	0.52	0.28	0.005	0.007	0.012	
Steel O	0.42	0.44	0.018	0.013	0.49	0.12	2.53	0.51	0.28	0.005	0.007	0.012	
Steel P	0.43	1.87	0.019	0.011	1.37	0.18	4.20	1.64	0.61	<0.005	<0.005	<0.005	
Steel Q	0.40	1.81	0.012	0.005	1.43	0.15	3.55	1.63	0.57	<0.005	<0.005	<0.005	
Steel R	0.39	1.56	0.011	0.005	1.03	0.16	3.83	0.94	0.6	<0.005	<0.005	<0.005	
Steel S	0.39	1.57	0.011	0.005	1.03	0.16	3.7	0.92	0.59	<0.005	<0.005	<0.005	
Steel T	0.39	1.59	0.012	0.006	0.45	0.16	3.66	1.41	0.61	<0.005	<0.005	<0.005	
Steel U	0.40	1.57	0.012	0.005	0.45	0.16	3.84	1.46	0.63	<0.005	<0.005	<0.005	
Steel V	0.40	2.08	0.01	0.008	0.98	0.17	3.76	1.00	0.57	<0.005	<0.005	<0.005	
Steel W	0.43	2.11	0.01	0.007	0.98	0.16	3.78	0.99	0.61	<0.005	<0.005	<0.005	

Table (4.3.32): Martensite start temperatures [°C] of the steels A through to O measured by dilatometry.

Steel	**A**	**B**	**C**	**D**	**E**	**F**	**G**	**H**
M_S [°C]	285	253	241	243	196	255	271	210
Steel	**I**	**J**	**K**	**L**	**M**	**N**	**O**	**P**
M_S [°C]	309	305	318	252	175	241	218	115
Steel	**Q**	**R**	**S**	**T**	**U**	**V**	**W**	
M_S [°C]	178	170	182	184	170	145	130	

Linear regression based on M_s measurements of these 23 armour steels without considering any interaction parameters between alloying elements showed that it is difficult to fit all the experimental data on the martensite start temperature with the chemical composition using one equation. The formula proposed by Wang gives good approximations only when the M_s of the armour steel is higher than 200°C. Above 0.40%C the differences from the measured values of M_s become larger than 100°C. The following approach was then suggested in this study for the estimation of the martensite start temperature of the steels with chemical compositions in the range considered.

$$M_S\left(^0C\right) = 548 - 590C - 35Mn - 18Ni - 14Cr - 9.5Mo - 12Si \qquad (4.14)$$

Formula (4.14) proposed in this work for the estimate of the martensite start temperature of the armour steels, is based on measured values within the range of chemical compositions of interest for ballistic performance steels. The chemical compositions of these steels are well within the specified ranges for the previous formulas (4.12) and (4.13), which makes the comparison between them valid.

4.3.7.1 Determination of the relationship between the chemical composition and the martensite start temperature proposed in formula (4.14)

After measuring the martensite start temperatures of the first 15 armour steels (Steels A through to O) their martensite start temperatures were fitted through multi-linear regression of the martensite start temperatures to the chemical compositions. The validity of each fitting was verified with the eight remaining steels. The three best fittings were considered in the prediction of the martensite start temperatures of the steels P through to W and the final equation was assessed through a comparison between the predicted and the measured values.

Table (4.3.34) Measured martensite start temperatures of six armour steels

Name of the steel	Martensite start temperature [°C]
B	253
G	271
H	210
I	309
J	306
K	318

The most likely elements in these steels to affect the M_s temperature are Carbon, Manganese, Silicon, Nickel, Chromium and Molybdenum. The hypothesis of the chemical composition dependency of the martensite start temperature of the steels may be expressed, without interaction parameters, as:

$$M_S\left[^0C\right] = 539 + a \times W_C + b \times W_{Mn} + c \times W_{Si} + d \times W_{Ni} + e \times W_{Cr} + f \times W_{Mo} \qquad (4.15)$$

where a, b, c, d, e and f are six regression parameter to be determined and W_C, W_{Mn}, W_{Si}, etc. are the mass percentages of the alloying elements in the armour steels. The

experimental values of the martensite start temperatures and the chemical compositions of the six steels were introduced into Equation (4.15). Therefore, a system of six equations with six unknowns, viz. the regression parameters, was developed. The corresponding matrix representation for the martensite start temperatures measured after austenitisation at 900°C, therefore, was:

$$\begin{bmatrix} -286 \\ -268 \\ -329 \\ -230 \\ -233 \\ -221 \end{bmatrix} = \begin{bmatrix} 0.317 & 0.855 & 0.176 & 3.8 & 0.318 & 0.367 \\ 0.37 & 0.40 & 0.43 & 2.8 & 0.24 & 0.3 \\ 0.37 & 1.15 & 1.06 & 3.8 & 0.52 & 0.43 \\ 0.34 & 0.39 & 0.40 & 2.43 & 0.27 & 0.37 \\ 0.3 & 0.48 & 0.35 & 1.4 & 0.48 & 0.19 \\ 0.30 & 0.65 & 0.75 & 2.83 & 0.84 & 0.45 \\ 0.30 & 0.97 & 0.93 & 4.1 & 0.83 & 0.69 \end{bmatrix} \times \begin{bmatrix} a \\ b \\ c \\ d \\ e \\ f \end{bmatrix} \quad (4.16)$$

The solution of the above system using the method of the inverse matrix, gives the regression factor vector:

$$\begin{bmatrix} -719 & -197 & 9.83 & 64 & 96 & -325 \end{bmatrix} \quad (4.17)$$

The components of the vector in Equation (4.17) are the coefficients to be averaged to obtain the coefficients in Equation (4.14). One should expect a dependence of these coefficients on the austenitisation temperature and time because of differing degrees of dissolution of alloy carbides; hence the martensite start temperature itself should be a tribute of the austenitisation parameters.

The graphical comparison between the measured and the predicted values using the three formulas for the 23 steels are compared in Figure 4.3.31. From Figure 4.3.31 it appears that the published Equation (4.12) leads to systematically higher estimates of the martensite start temperatures than the measured values. For the armour steels whose martensite start temperatures are between 200°C and 318°C, the formulas (4.13): published) and (4.14): proposed) give comparable results close to the experimental values. But at martensite start temperatures lower than 200°C the published formula (4.13) deviates from the experimental values whereas the proposed formula (4.14) still gives good agreement between measured and predicted values. However, at low martensite start temperatures the formula (4.14) also results in larger differences between the experimental and the predicted values. This suggests that the effects of the alloying elements on the martensite start temperatures of these steels is not necessarily linear. Moreover, the predictive models of the martensite start temperature should possibly be defined for either the low (plate martensite) or the high martensite start temperatures (lath martensite).

A single model that uses the estimates of martensite transformation temperatures for both plate and lath martensite may deviate at one end of the temperature scale. Secondly, Nitrogen (that has not been included in this analysis) may also modify the magnitudes and the signs of the regression coefficients in these formulas substantially. The standard deviation is 52°C for the published formula (4.12), 34°C for the published formula (4.13) and only 19°C for the proposed formula (4.14).

Table 4.3.34. Measured and estimated values of the martensite start temperatures of 23 armour steels

	Martensite start temperature {°C]			
Steel designation	**Measured**	**(Eq 4.14 proposed in this study**	**Wang**	**Stevens**
A	285	218	266	287
B	253	255	241	315
C	241	251	261	318
D	243	247	268	318
E	196	185	117	261
F	255	221	271	294
G	271	254	289	321
H	210	189	212	263
I	309	271	298	331
J	306	308	315	363
K	318	264	259	323
L	259	225	213	288
M	175	131	110	216
N	241	203	237	280
O	218	215	247	291
P	115	100	35	191
Q	178	131	58	217
R	170	155	128	235
S	182	158	129	238
T	184	158	84	236
U	170	148	78	228
V	145	132	78	216
W	130	112	73	215

Theories on the chemical composition dependency of the martensite start temperature of steels, stipulates that the substitutional elements Mo, Mn, Ni, Cr and Si have different effects on the proof stress of the austenite matrix due to differences in the misfit strain and the chemical bond energies.

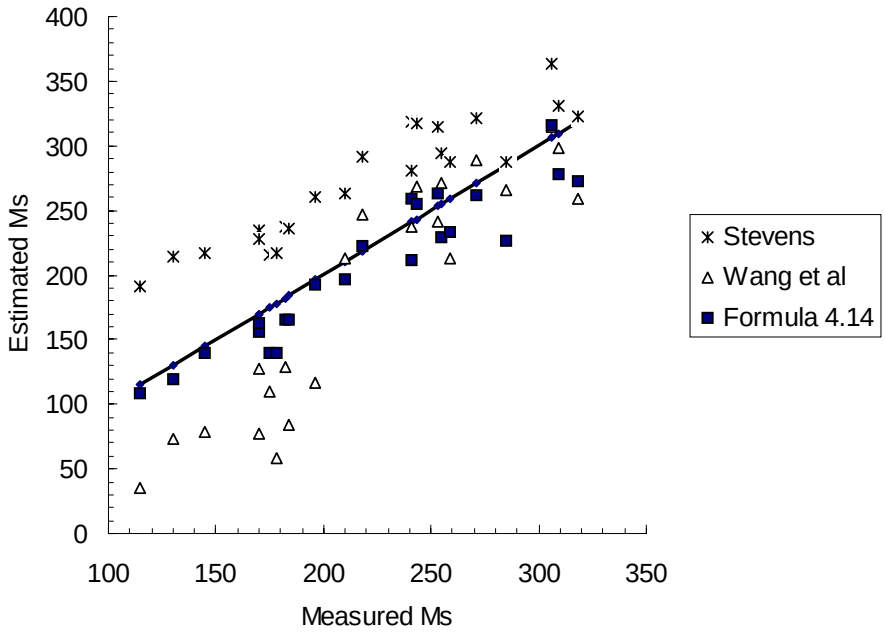

Figure 4.3.31: Comparison between the measured and the predicted martensite start temperatures for the 23 experimental alloy steels. The predictions were from the published empirical formulas (4.12), (4.13) and the proposed empirical formula (4.14) for armour steels is also shown. The diagonal represents the measured values

The strengthening of the austenite matrix will require a larger driving force for its decomposition into martensite since the transformation front has to move through a hardened matrix, giving rise to a decrease in the martensite start temperature. However, Schramm and Reed [21] reported that both Mn and Mo increase the stacking fault energy of the austenite matrix, although most substitutional elements are generally considered to lower the stacking fault energy of the austenite matrix, allowing stacking faults to separate further making cross slip of screw dislocations more difficult.

A least squares fitting applied to the above three formulas for the 23 armour steels of this study, gives the following values that show a better agreement between the measured martensite start temperatures and the predicted values using formula (4.14).

Table (4.3.35): Sum of squared differences between measured and calculated values of the M_s for the 23 steels (steel A through to W)

Sum of the squared differences		
Formula (4.12)	**Formula (4.13)**	**Formula (4.14)**
72651	70670	13578

Stevens (formula 4.12) reported that Cobalt increases the martensite temperature and Aluminium may have the same effect. The monotonic decrease of the martensite start temperature with the alloying element content should then be considered as a particular case and not as a rule. The multiplying factors are strongly dependent on the chemical

composition ranges, the austenitisation temperature and the technique used for the measurement. The acoustic technique, for example, detects the formation of the very first plates of martensite and generally gives higher values of the martensite start temperature whereas optical metallography is less sensitive and gives lower values of the M_s. In turn, the multiplying factor in a predictive formula will also change.

4.3.7.2 Effect of the austenitisation temperature on the M_s temperature

The effect of the austenitisation temperature on the martensite start temperature was analysed for seven armour steels selected from the twenty-three experimental steels. The martensite start temperatures of the steels E, F,G, H, J, M and N are presented in Table 4.3.36 for four different austenitisation temperatures.

Table (4.3.36): Martensite temperatures of seven steels as a function of the austenitisation temperature

	Martensite start temperature [°C]						
Austenitisation temperature	**Steel E**	**Steel F**	**Steel G**	**Steel H**	**Steel J**	**Steel M**	**Steel N**
800°C	193	244	278	202	299	187	241
850°C	189	244	275	205	305	176	239
900°C	196	255	282	210	308	175	238
950°C	187	248	271	193	293	169	233

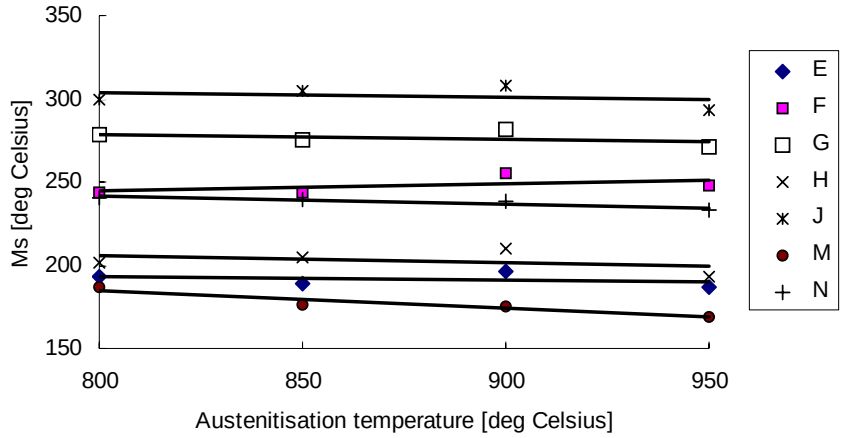

Figure 4.3.32: Effect of the austenitisation temperature on the M_s of seven armour steels

The martensite start temperatures of these armour steels appear to slightly decrease when the austenitisation temperature is increased from 800°C to 950°C. The increase in the austenitisation temperature has many consequences, i.e. greater dissolution of carbides, solid solution hardening of the parent austenite and grain growth and all of these may modify the thermodynamic as well as the kinetic characteristics of the transformation. Greater dissolution of the carbides changes the chemical composition of the matrix and, hence, the chemical driving force for the transformation to martensite. It also increases the

solid solution hardening of the parent austenite, which affects the movement of the transformation front through the austenite.

4.3.7.3. Steel composition considerations

From the preceding paragraphs it may be concluded that the following chemical composition factors are to be noted in designing an improved armour steel:

a. Carbon is the main element determining the hardness of the martensite. A hardness higher than 500 VHN may be obtained when the Carbon content of the armour steel is above 0.37 wt%C as established in Sections 4.1 and 4.2.

b. It appears that the Silicon content of the steel has a strong effect on the stability of the martensite upon tempering as shown in Table (4.3.37) for five armour steels from this study. Silicon delays the softening of the martensite during tempering to higher temperature.

Table (4.3.37): Silicon content and the temperature of softening of the martensite in five experimental steels

Steel	Si	Cr	Ms	Temperature of start in decrease in mechanical properties
E	0.21	1.49	196°C	200°C
F	0.8	0.22	255°C	250°C
G	0.43	0.24	271°C	150°C
H	1.06	0.52	212°C	300°C
I	0.40	0.27	309°C	200°C

Silicon increases the stability of the martensite by reducing the chemical activity of carbon [75, 77, 80]. Silicon becomes effective in delaying the decomposition of the martensite in the range between 0.5 wt% to 1.0 %C. The combined effect of Silicon and Chromium presents a maximum effect at 1.5 wt%(Si+Cr). In these steels the martensite remains stable in an "untempered" condition below 150°C. Further Silicon additions may increase this temperature up to 300°C.

c. The fractographs of the shear lips from the Charpy and tensile tests have shown a detrimental effect of elongated particles of MnS under impact as well as under tensile stress. Sulphur should therefore be kept below 0.003 wt%S for these steels. The shape of the MnS particles is strongly dependent on the Oxygen content of the solidifying steel. A lower Oxygen content will favour the less detrimental equi-axed shape.

d. The samples austenitised at 900°C, quenched in water at room temperature and then polished electrolytically in a 5% percholric acid and 95% glacial acetic acid solution were analysed by XRD for a semi quantitative analysis of the retained austenite.

e. The ideal alloy should be Titanium-, Niobium- and Aluminium-free to avoid the risk of cracking initiation near the coarse inclusions or precipitates.
For the steels with 0.37%C to 0.39%C and 0.5 %Si to 1.0%Si, the tempering heat treatment should be kept below 200°C to achieve both hardness (500– 600 VHN) and tensile strength between 1300 and 2200 MPa. Tempering above 250°C is not acceptable because of the lower hardness that results. In these conditions the impact energy of the sub-sized specimens at -40°C is in the range 10 to 18 Joules.

f. The martensite start temperature of the armour steels may be approximated with acceptable accuracy using the formula (4.14)

4.4. Results of the ballistic testing (First series)

4.4.1. Ballistic report

The first series of ballistic testing was done on five plates of which two of steel E, one of steel F, one of steel G and one of steel H and their results are reported in Table 4.4.37. The second plate of steel E was tested from a firing distance of only ten meters which is significantly less than the specified thirty meters. The plates that were considered to have passed the ballistic test, had to resist penetration after at least five shots. The parameters and effect of each shot was recorded. No light should be visible through the impacted region for the shot as having been resisted and the test to be considered as having passed. The 5.56 mm projectiles used for the ballistic testing are presented in Figure 4.4.33.

Ball | High Pressure | Tracer | SS109

Figure 4.4.33: 5.56 mm rounds fired by a R4 during the ballistic test (first series)

The mechanical properties of the first series of five armour steel plates mentioned above, are as follows:

Table (4.4.37): Properties of the plates austenitised at 900°C for 1 hr and tempered at 180°C for 1 hr before the first series of ballistic testing

	Thickness [mm]	Vickers Hardness	YS [MPa]	UTS [MPa]	YS/UTS	Retained austenite [%]	Elongation [%]	Impact energy at –40 [Joules]	Martensite start temperature [°C]
Steel E	6.2	578	880	1780	0.50	6	4	10	196°C
Steel F	6.2	610	1500	2200	0.68	0.6	8	14	255°C
Steel G	6.1	475	1500	2000	0.75	0.6	12	17	271°C
Steel H	6.1	565	1100	1897	0.58	4	6	14	210°C

In the above table the Charpy impact energy was measured on the sub-sized specimens of $5 \times 10 \times 55$ mm. The comparison of the ballistic performances of these plates is shown in the next Section and the validity of the prediction models discussed.

Typical images of the plates after ballistic testing are presented in Figure 4.4.34. The visual analysis of the rear face of the plate of steel E in Figure 4.4.34(b) does not show any sign of deformation due to the ballistic impact. This observation led to decreasing the firing distance to ten meters for the second plate of steel E. This observation was also instrumental in redesigning the alloys in the next series for the advanced performance armour plates.

Table 4.4.38: Ballistic report (first series)

Plate designation		Firing Distance (Meter)	Firing Angle (°)	Hardness Vickers	Measured projectile velocity (m/s)	Ballistic performance
Name	Thickness [mm]					
Steel E	6.2	30	0	578	943	Passed well
					951	Passed well
					956	Passed well
					952	Passed well
					987	Passed well
Steel E	6.2	10	0	578	-	Passed well
					-	Passed well
					-	Passed well
					-	Clean Penetration
					-	Clean Penetration
Steel F	6.2	30	0	610	954	Clean Penetration
					942	Clean Penetration
					957	Clean Penetration
					944	Passed well
					952	Passed well
Steel G	6.1	30	0	475	948	Clean Penetration
					955	Clean Penetration
					947	Clean Penetration
					933	Clean Penetration
					948	Clean Penetration
Steel H	6.1	30	0	535	1013	Passed well
					951	Bulge + Crack + No light penetration
					947	Passed well
					956	Passed well
					940	Passed well

4.4.34(a): Front face of steel E

4.4.34(b): Rear face of steel E

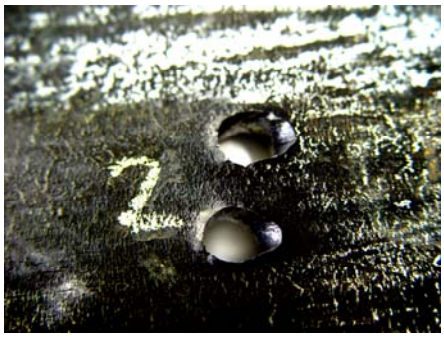

4.4.34(c:). Front of Steel F plate after firing

Figure 4.4.34: (a) and (b) Front and rear faces of the plate of steel E showing good resistance to the ballistic impact after being fired from 30 meters. 4.4.34(c) : Front face of the plate of steel F showing the clear penetration holes and the elevated contours at the edges of the penetration due to the compressive stresses in the incidence region.

4.4.2. Comparison with the ballistic performance specifications

In the following sub-sections, results of the first series of ballistic testing, reported in Table 4.4.38 are compared to the prediction using two different criteria, one reported in the literature and one specified by ARMSCOR and Mittal Steel (South Africa); and a third improved criterion from this study is proposed.

4.4.2.1. The Ballistic Performance Index (BPI).

The Ballistic Performance Index introduced by Srivathsa and Ramakrishnan [6,7] has been defined in Sub-section 2.2.4. Although the knowledge of the relationship between the mechanical properties and the ballistic performance of steels is still lacking, the BPI constitutes an attempt to quantify and to be able to compare such performance for two armour materials. The BPI does not consider the hardness as a determining factor for the ballistic performance. This is totally different for the specification used by Mittal Steel (South Africa) where the high hardness of the steel plate is the major criterion in predicting the resistance to ballistic impact.

The BPI of the steels E, F, G and H calculated according to the above-mentioned model are shown in Table 4.4.39. For this calculation a minimum muzzle velocity of 940 m/s is considered. The Young's modulus of the steels is assumed to equal 200 GPa and the density equal to 7800 kg/m^3.The reductions in area after tensile testing were respectively 6%, 11%, 20% and 8% for these four steels.

Table 4.4.39: The ballistic Performance Index of the steels E, F, G and H

	Steel E	Steel F	Steel G	Steel H
BPI	3.7	3.9	4.6	4.5

It is concluded from this table that the BPIs of these four steels are very close but with a tendency to higher values for the steels with higher strength, which is contradictory to the experimental observation on these four steels.

The formula for the BPI has the value of taking into account the effect of the reduction in area on the ballistic performance. It shows the tendency for localised yielding in steels with a large reduction in area that leads to poor ballistic performance. The formula of the BPI also demonstrates the decrease in ballistic performance when the velocity of the fired round increases. In the case of these four steels the BPI is multiplied by 3 to 4 when the velocity of the round is reduced from 940 to 400 m/s. But the BPI still seems to predict a higher performance for steels that have a higher strength which the authors themselves disproved from their experience and is also contradictory to the ballistic results of this study in Table (4.4.39).

The assessment of performance by ballistic testing remains indispensable and confirms the current observation that a clear relationship between the mechanical properties and the ballistic performance is still lacking. The Ballistic Performance Index should then possibly be considered only as a qualitative indication of ballistic performance and may be used for the comparative selection between different armour materials only when the BPIs are different by more than a margin or a ratio yet to be determined.

4.4.2.2. The Mittal Steel (South Africa) specifications

From the current specifications for military applications of armour steels, Mittal Steel (South Africa) has determined the specification limits for the advanced performance armour steel to be developed in this study, as follows [1]:

- the hardness is the main factor determining the ballistic performance and should be higher than 600 BHN, that is equivalent to 640 VHN;
- the Charpy impact energy of the full size specimen at -40°C should be higher than 13 Joules;
- the yield strength of the steel should be higher than 1500 MPa;
- the ultimate tensile strength should be higher than 2000 MPa; and
- the minimum elongation of a 50 mm gauge is fixed at 6%.

According to this specification the prediction of the ballistic performance is favourable for steel F only. However, the result from the ballistic testing is uncertain because the plate of this steel resisted two shots well but three others penetrated the plate. On the other hand steels E and H passed the ballistic test well despite the lower hardness and tensile properties than specified. Steel G satisfied all the aspects of the specification except the main one, i.e. the hardness, and it failed the ballistic test. One should conclude then that the high yield strength, the high tensile strength, the high elongation and the high impact energy of steel G did not play a decisive role in resisting high velocity impacts.

4.4.3. Differences in the microstructures between steels E, F, G, H and I

This paragraph aims to define a *direct relationship* between the microstructure and the ballistic performance instead of to seek an *indirect relationship* via the mechanical properties. The microstructures and the phases present in these four armour steels before ballistic testing were analysed in thin foil transmission electron microscopy, in atomic force microscopy and X-ray diffraction. The X-ray diffraction allowed the determination of the volume fraction of the retained austenite as well as the lattice parameters of both the martensite and the retained austenite. In this paragraph the differences in microstructures and phases are considered and used to explain directly the observed differences in ballistic

performance of the above steels. Further characterisation of the martensite will be done in Chapter 6.

The measured volume fraction of the retained austenite in these five steels and their martensite start temperatures were found to be:

Table (4.4.40): % Retained austenite in steels E, F, G, H and I after water quenching from 900°C

	Steel E	Steel F	Steel G	Steel H	Steel I
Retained austenite [%volume]	6	0.6	0.5	2	0.5
Martensite start temperature	196	255	271	210	309

The detection limit for retained austenite of the X-ray equipment used is generally less than 2% volume fraction, below which the volume fraction may not be quantified accurately. From Table (4.4.40) it may be seen that the 6 mm armour plates of the Group 1 alloys contains detectable amounts of retained austenite and these steels have passed the ballistic test while those with non-detectable retained austenite failed the test.

It may also be observed from Table (4.4.37) that steels E and H have values of the yield strength to ultimate tensile strength ratio smaller than 0.6. The low value of the YS/UTS ratio indicates a resistance against localised yielding; in other words, it indicates the ability of the material to dissipate the impact energy transversally to the incidence direction of the fired round in the plate . This property increases the volume of the material interacting with the fired round, offering better resistance to perforation. The elongation during uniaxial tensile testing also indicates the tendency for localised yielding of the steel when impacted. It should be kept lower than 7%, which is contrary to the specification used by Mittal Steel (South Africa).

The different types of morphologies of the martensite in these five steels are shown in the following figures where they are arranged in order of increasing martensite start temperature.

The untempered steels E and H contain twinned martensite and nodular particles of retained austenite (RA), as shown in Figures 4.4.35(a) and (b). The size of the RA nodules allow their detection by X-ray diffraction analysis. The twins run across the entire width of the martensite plates. No traces of auto-tempering were observed throughout the thin foils under 18000 to 43000 magnification. Steels F and G on the other hand contain lath martensite with high dislocation densities within the laths. They also contain thin films of retained austenite along the lath inter-faces, as shown in the dark field thin foil electron micrograph in Figures 4.4.35(c) and (d). The volume fraction of retained austenite in these two steels was estimated to be less then 0.6%. The bright field transmission electron micrographs of the quenched specimens of steels F and G also contain areas with fine carbides along the lath inter-faces. In these steels with intermediate martensite start temperatures, auto-tempering due to the relatively rapid diffusion of the Carbon atoms and the subsequent formation of fine cementite particles, could not be avoided during the

quenching. This observation was also mentioned earlier by Krauss [51] for steels of which the martensite start temperatures are well above room temperature.

Figure 4.4.35(e) is a thin foil bright field image of steel I of which the martensite start temperature is relatively high, i.e. 309°C. The martensite in this steel consisted of large laths which were less dislocated, possibly due to enhanced annealing of the dislocations and the large plastic accommodation across the reaction front during the martensitic transformation at this high temperature. The laths are large and contain large areas with fine cementite particles that are not confined to the lath interfaces as was the case in steels F and G. This microstructure of steel I presented the lowest hardness, the highest impact energy and the largest elongation among the five steels discussed here. The tensile properties of steel I were also measurable in the quenched condition that was not the case for steels E and H.

From the morphology, M_s temperatures, Silicon contents of these steels and the evidence obtained in indexing some SADPs of these steels (see later in Section 6.4) as well as the fact that these dark field micrographs were obtained from untempered steels and hence could only possess very minor quantities of autotempered carbides in the high-M_s temperature steels, it is concluded that the dark field micrographs in Figure 4.4.35 do represent the retained austenite.

The surface relief of these five steels after quenching and analysed in simple contact atomic force microscopy shows, likewise, as in transmission electron microscopy, a change in the morphology from the sheared twinned martensite to the dislocated and the plastically accommodated lath martensite as the martensite start temperature increased. The Figures 4.4.36(a) through to (d) present the surface relief evolution for these five steels, once more arranged by increasing martensite start temperatures. These measurements to analyse the characterisation of the twinned and the lath martensite with respect to their surface relief, are presented in Chapter 6. Olson [58] reported that the morphology of the retained austenite within laths or plates, determines whether the austenite will transform by a stress- or strain-induced mechanism to martensite.

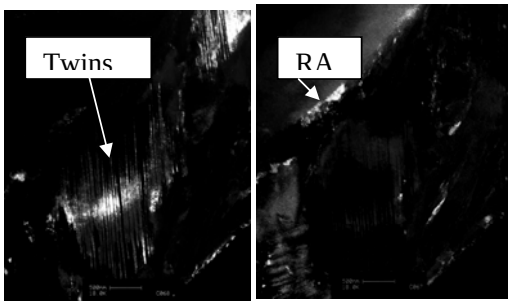

Figure 4.4.35(a): Steel E, M_S=196°C

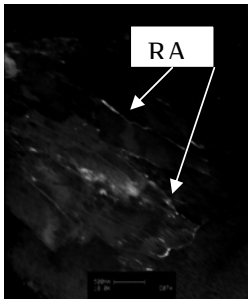

Figure 4.4.35(b): Steel H, M_S=210°C

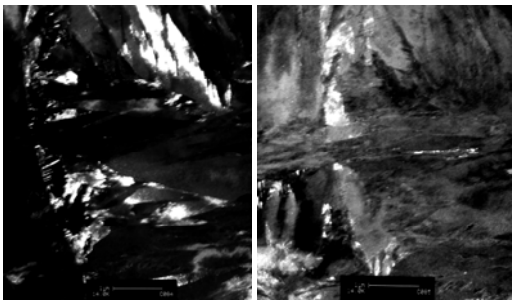

Figure 4.4.35(c): Steel F, M_S=255°C (label 500 nm)

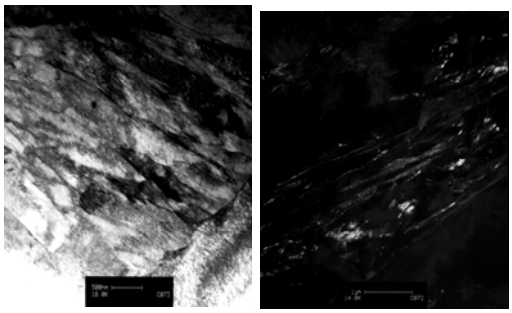

Figure 4.4.35(d): Steel G, M_S=271°C

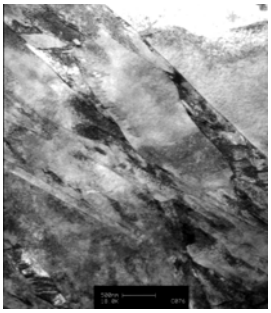

Figure 4.4.35(e): Steel I, M_S=309°C (label 500 nm)

Figure 4.4.35: Thin foil transmission electron micrographs (x 10000, label 500 nm) showing the morphology of the martensite and retained austenite in steels E through to I after water quenching from 900°C.

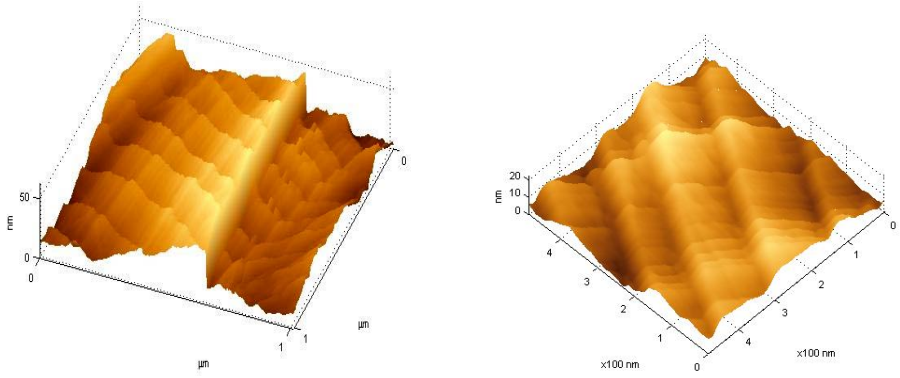

Figure 4.4.36(a): Steel E, M_S = 196°C, twinned martensite

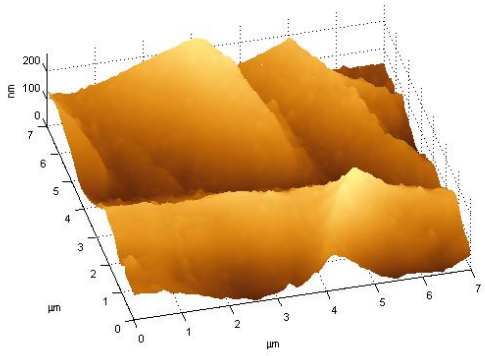

Figure 4.4.36(b): Steel H, M_S = 210°C, sharp edges and regular N-shaped surface of twinned martensite without sheared micro-twins

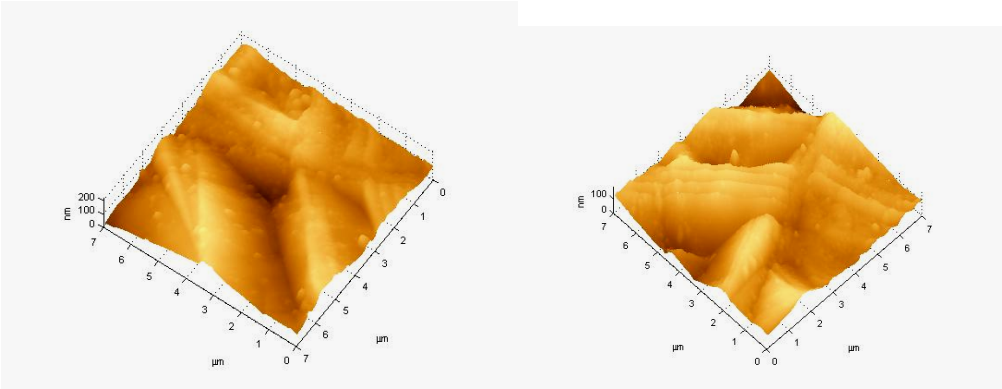

Figure 4.4.36(c): Steel F, M_S = 255°C, lath martensite with rounded edges

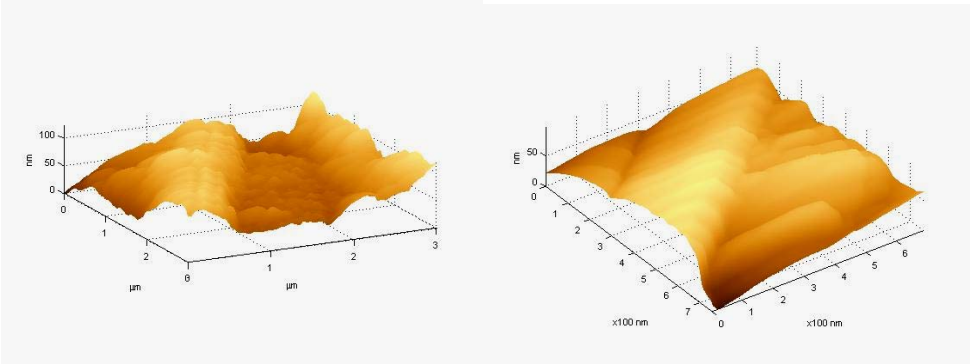

Figure 4.4.36(d): Steel G, M_S = 271°C, background of lath martensite that contains some twins

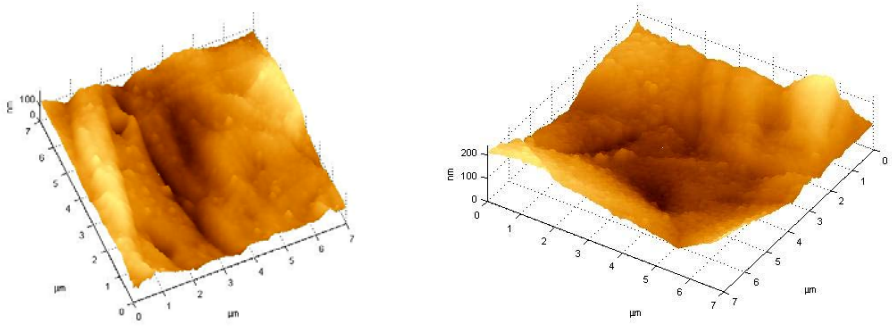

Figure 4.4.36(e): Steel I, M_S = 309°C, lath martensite. Surface showing plastic strain accommodation

Figure 4.4.36: Atomic force microscopy of the surface relief of steels E to I.

Figure 4.4.36 demonstrates that atomic force microscopy is a useful complementary technique that may be used in characterising the martensite. It does suffer from two deficiencies however. (1) The relief of peaks of the martensite plates formed at high M_s temperatures, may be blunted somewhat through rapid surface diffusion of atoms before reaching room temperature where the relief measurements are actually carried out. (2) The martensite formed at a free surface is only partially restrained whereas that formed within the volume of the microstructure is fully hydrostatically restrained. This difference may place some question marks on conclusions derived from surface relief measurements.

Surface relief measurements nevertheless constitute a complementary contribution to a study of the internal details revealed by the thin foil transmission electron microscopy. Indeed Figure 4.4.36(a) demonstrates the formation of martensite with micro-twins within the plate martensite. This mechanism of formation is one of those predicted by the crystallographic theory of the martensitic transformation. The amplitude of the plastic strain accommodation during the martensitic transformation increases as the martensite start temperature increases. The mechanism of formation of the martensite seems to be a shear when the martensite start temperature is lower than 210°C as shown in Figure 4.36(b). For the martensite start temperatures of 255°C and 271°C, the twinned martensite was formed as plate martensite with their shape no longer regular with sharp edges as was the case in Figures 4.4.36(a) and 4.36(b). These irregular shapes may be related to a significant rotation of the habit plane during the martensitic transformation, although the possibility of surface diffusion may also have made some contribution. This observation on the rotation of the habit plane is in good agreement with the earlier conclusions in the literature by Mou and Aaronson [21] on a change in the mechanism of martensite formation and the coexistence of both lath and plate martensite when the martensite start temperature is about 250°C.

The data reported in Table (2.7) show that the two types of martensite may be formed together in a wide range of martensite start temperatures ranging from 200°C to 390°C. In this range of martensite start temperatures both the shear mechanism and the plastic accommodation of the deformation strain by slip and rotation of the habit plane are operative. This combined mechanism produces irregular N-shaped profiles that indicate irregular habit planes and is in agreement with the conclusion by Kennon and Dunne [46,

49] about the flexibility of the habit plane that is likely to be a characteristic feature of the plate martensite not accounted for by the crystallographic theories. Tadaki and Shimizu [48] also suggested that the formation of a continuous spectrum of habit planes should be expected based on their measurements of the variation of the lattice parameters of the martensite and the retained austenite as a function of the actual temperature of formation. The topology of the surface of steel I, in Figure 4.36(e), of which the martensite start temperature was 309°C, can be interpreted that the plastic strain accommodation results from the slip of dislocations.

4.4.4. Differences in microstructure between steels E, F, G, H in the tempered condition before ballistic testing

Thin foil transmission electron micrographs of the tempered armour steels E , F, G and H before ballistic testing, are compared in Figures 4.4.37(a) through to 4.4.37(d). The steel plates were tempered at 180°C for one hour. Fine elongated strings of carbides were found to have precipitated within steels E and H respectively, as shown in Figures 4.4.37(a) and 4.4.37(b). These two steels passed the ballistic testing well. On the other hand, coarse carbides have precipitated within the laths and on the lath interfaces of steels F and G that gave poor ballistic performances.

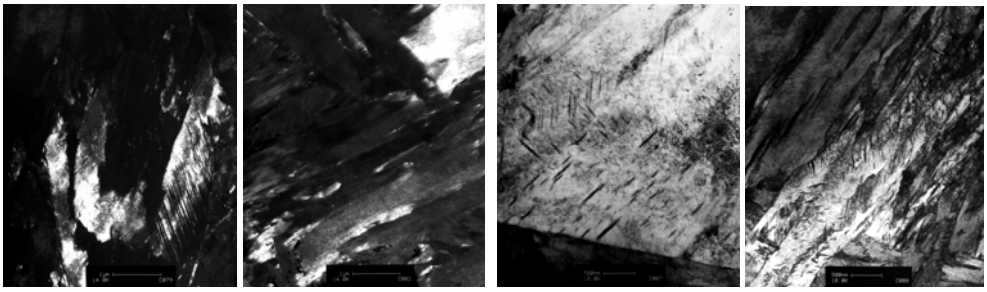

4.4.37(a) 4.4.37(b) 4.4.37(c) 4.4.37(d)

Figure 4.37: Thin foil transmission electron microscopy of the steels E (4.4.37(a)), steel F (4.4.37(b)), steel F (4.4.37(c)) and steel H (4.4.37(d)) after tempering at 180°C (label scale = 500 nm).

A high ballistic performance requires a microstructure consisting of twinned martensite with some retained austenite without coarse carbides. The precipitation of cementite may be controlled by the chemical composition of the armour steel and by the tempering temperature.

Steels E and H that gave good ballistic performances after tempering at 180°C for one hour, were then tempered at a higher temperature of 350°C for 1 hour with a view to determine the maximum tempering temperature that does not lead to the precipitation of the coarse cementite which is detrimental to the resistance to high velocity impact during ballistic testing. The thin foil micrographs in Figure 4.4.38 show large strings of cementite that had formed along the plate interfaces of steel E, shown in Figure 4.4.38(a) while steel H had formed noticeably less of these coarse strings of carbides during tempering at 350°C.

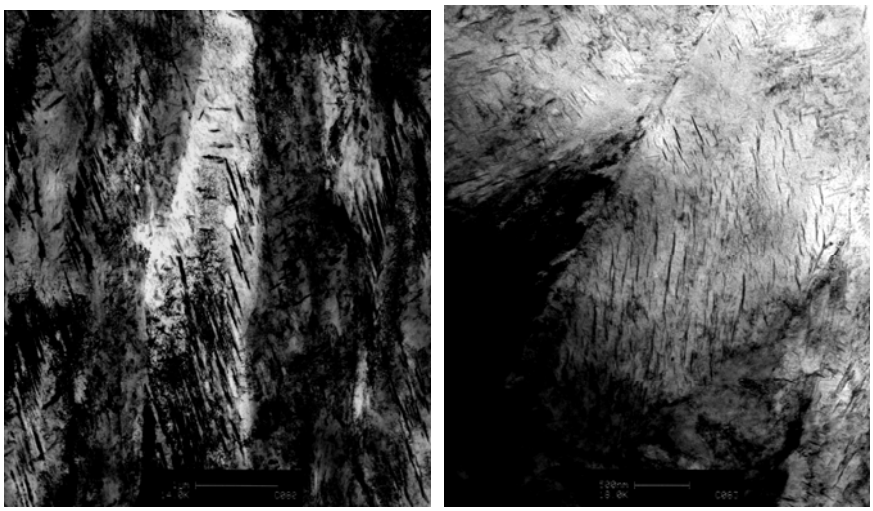

4.38(a): Steel E **4.38(b):** Steel H

Figure 4.4.38: Bright field thin foil transmission electron micrographs (x18000) of steels E and H after tempering at 350°C (label scale = 500 nm).

The retardation in formation of cementite during tempering of steel H may be attributed to its higher Silicon content of 1.06%, compared to the lower Silicon content of steel E of 0.21%Si. Silicon is well known for its effect on delaying the formation of cementite from supersaturated metastable martensite.

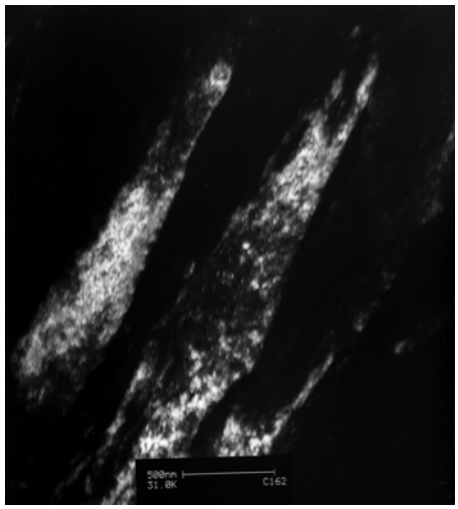

Figure 4.39: Thin foil TEM DF of steel E tempered at 400°C showing the cementite precipitated within the plates

Figure 4.4.40: Bright field thin foil transmission electron microscopy of steel H tempered at 300°C showing the cementite

Figure 4.4.41: Bright field thin foil transmission electron microscopy of steel E tempered at 400°C showing large strings of the cementite.

4.4.2.3. Proposition to redefine the specification of armour plate steels

Considering that neither the high hardness nor the higher levels of mechanical properties (yield strength, ultimate tensile strength, impact energy, % elongation) appear to be accurate criteria for predicting the ballistic performance of armour steels, an alternative design methodology is proposed. Those new design criteria are based on the results of this study of ballistic testing, the mechanical properties and the microstructure of the martensite.

This design approach is developed by also considering the volume fraction of retained austenite, the ratio of yield strength to ultimate tensile strength and the martensite start temperature of the five plate armour steels tested. The new proposal is derived from Tables 4.4.37 and 4.4.38 in which the steels E and H of the Group 1 armour steels, gave superior ballistic results, whereas steel G of Group 3 gave poor ballistic results and steel F of Group 2 gave intermediate ballistic results.

The new specifications should, therefore, rather prescribe the following:

- the volume fraction of retained austenite in the martensitic steel should be between 2% and 7%;
- the ratio of yield strength to ultimate tensile strength should be less than 0.6;
- the martensite start temperature should ideally be comprised in the range from 130°C to 220°C. The martensite start temperature may be determined by dilatometric analysis or predicted (with an error of ± 30°C) using the empirical Formula (4.14) derived from this study;
- the chemical composition should be close to that of steels E and H, i.e. 0.39%C, 1.2%Mn, 0.8%Si, 1.5%Cr, 0.5%Mo, 2.5%Ni.
- The austenitisation temperature between 850 and 950 for 30 minutes to one hour
- The tempering treatment at temperatures lower than 250 for 15 minutes to 1 hour